



### 저작자표시-비영리-변경금지 2.0 대한민국

이용자는 아래의 조건을 따르는 경우에 한하여 자유롭게

- 이 저작물을 복제, 배포, 전송, 전시, 공연 및 방송할 수 있습니다.

다음과 같은 조건을 따라야 합니다:



저작자표시. 귀하는 원 저작자를 표시하여야 합니다.



비영리. 귀하는 이 저작물을 영리 목적으로 이용할 수 없습니다.



변경금지. 귀하는 이 저작물을 개작, 변형 또는 가공할 수 없습니다.

- 귀하는, 이 저작물의 재이용이나 배포의 경우, 이 저작물에 적용된 이용허락조건을 명확하게 나타내어야 합니다.
- 저작권자로부터 별도의 허가를 받으면 이러한 조건들은 적용되지 않습니다.

저작권법에 따른 이용자의 권리와 책임은 위의 내용에 의하여 영향을 받지 않습니다.

이것은 [이용허락규약\(Legal Code\)](#)을 이해하기 쉽게 요약한 것입니다.

[Disclaimer](#)



Master's Thesis

석사 학위논문

**Shape and size controlled synthesis of  
FePt and Ferrite nanoparticles for bio-applications**

Yun Ji Eom (엄 윤지 嚴允志)

Department of Emerging Materials Science

신물질과학전공

DGIST

2016

# **Shape and size controlled synthesis of FePt and Ferrite nanoparticles for bio-applications**

Advisor: Professor : Cheol Gi Kim

Co-Advisor: Professor Jong Soo Lee

By Yun Ji Eom

Department of Emerging Materials Science

DGIST

A thesis submitted to the faculty of DGIST in partial fulfillment of the requirements for the degree of Master of Science in the Department of Emerging Materials Science. The study was conducted in accordance with Code of Research Ethics<sup>1)</sup>.

01. 07. 2016

Approved by

Professor Cheol Gi Kim (\_\_\_\_\_)

(Advisor)

Professor Jong Soo Lee (\_\_\_\_\_)

(Co-Advisor)

- 1) Declaration of Ethical Conduct in Research: I, as a graduate student of DGIST, hereby declare that I have not committed any acts that may damage the credibility of my research. These include, but are not limited to: falsification, thesis written by someone else, distortion of research findings or plagiarism. I affirm that my thesis contains honest conclusions based on my own careful research under the guidance of my thesis advisor.

# **Shape and size controlled synthesis of FePt and Ferrite nanoparticles for bio-applications**

**Yun Ji Eom**

Accepted in partial fulfillment of the requirements  
for the degree of Master of Science.

01.07.2016

Head of Committee \_\_\_\_\_ (인)

Prof. Cheol Gi Kim  
(DGIST)

Committee Member \_\_\_\_\_ (인)

Prof. Jong Soo Lee  
(DGIST)

Committee Member \_\_\_\_\_ (인)

Dr. Eun Joo Kim  
(DGIST)

MS/EM      업윤지. Yun Ji Eom. "Shape and size controlled synthesis of FePt and Ferrite  
201421010     nanoparticles for bio-application". Department of Emerging Materials Science.  
2016. 50 p. Advisors Prof. Cheol Gi Kim, Prof. Co-Advisors Jong Soo Lee.

## Abstract

Magnetic nanoparticles (MNPs) with uniform shape and size distribution have been the great importance in various fields of applications, including magnetic energy, data storage, magnetic separation, drug delivery and biology applications. On the same time controlling the shape and size of the nanoparticles will have a significant effect on its various properties and consequently the potential applications. Therefore, various approaches like sonochemical, polyol, hydrothermal synthesis, microemulsion, thermal decomposition, and co-precipitation method have been developed for the nanoparticles morphology control. Among these approaches, the thermal decomposition route is considered the most attractive method for synthesis of high crystalline and uniform particle size distribution. However, the extent of control over particle dispersion and morphology was not adequate for achieving particles useful in real applications. In this thesis, I present a facile, safe, and convenient thermal decomposition route for morphology controlled synthesis of two kinds of ferrite nanoparticles ( $\text{Fe}_3\text{O}_4$  and  $\text{CoFe}_2\text{O}_4$ ) and one kind of magnetic alloy nanoparticles (FePt) for using in bio-medical applications.

For the ferrite nanoparticles, simple modification of the reaction condition, including temperature, time, solvent, surfactant, and precursor amount allowed us to isolate nanoparticles as cubes, hexagons and spheres ferrite NPs with broad sizes ranging. Oleic acid and oleylamine were used as the solvents, stabilizers, and reducing agents and iron(III) acetylacetone and cobalt(II) acetylacetone were successfully employed as precursors instead of commonly used toxic, flammable and expensive pentacarbonyl.

On the other hand, for FePt alloy nanoparticles, we could control the Fe atomic composition in FePt particle and two kind of structure which are homogeneous FePt and heterodimer structure (FePt/Fe<sub>3</sub>O<sub>4</sub>). For controlling the FePt alloy nanoparticles, we found that both of the reducing agent and precursor molar ratio are important parameter. First, using 1,2-hexadecanediol, when precursor mole ratio (Fe:Pt) increase from 1:1 to 3:1, Fe composition also increased. However, there are no more increase of Fe composition when used 4:1 molar ratio and also the heterodimer structures of Fe<sub>3</sub>O<sub>4</sub>/FePt is formed. On the other hand, when 1-octadecene, was used, no hetero structure even over 4:1 molar ratio is formed and also the controlling of FePt atomic composition ratio is more easier than the case of using 1,2-hexadecanediol.

Since the bio-compatibility is one of the important issues from the view point of practical bio-application, my thesis also focused on studying the effect of concentration of the synthesized FePt nanoparticles on the cytotoxicity of CCK-8 assay and Live/Dead cell through staining & confocal microscopy images. The cell survival rate increased with the culture days increased and concentration. 80% cell viability was maintained in less than 1000 µl/ml concentration and therefore the possibility for using our nanoparticles in the bio- application was confirmed from these data.

## **Keywords**

Synthesis of magnetic nanoparticles, Fe<sub>3</sub>O<sub>4</sub>, CoFe<sub>2</sub>O<sub>4</sub>, FePt, FePt/ Fe<sub>3</sub>O<sub>4</sub>, bio-application

## Contents

<b>Abstract .....</b>	i
<b>List of contents.....</b>	iii
<b>List of figures.....</b>	iv
<b>I . Introduction.....</b>	1
<b>II. Research background.....</b>	4
2.1. Magnetic nanoparticles.....	4
2.1.1. Ferrite.....	4
2.1.2. Other types of ferrites.....	6
2.2. Magnetic properties.....	8
2.2.1. Superparamagnetism.....	8
2.2.2. Anisotropy.....	12
2.3. Synthesis method of magnetic nanoparticles.....	13
2.3.1. Co-precipitation.....	13
2.3.2. Thermal decompostion.....	15
2.3.3. Formation of nanoparticles.....	16
2.4. Characterization.....	18
2.4.1. Transmission Electron Microscopy.....	18
2.4.2. X-ray diffraction.....	18
2.4.3. Vibrating Sample Magnetometer.....	19
<b>III. The synthesis of Fe<sub>3</sub>O<sub>4</sub> and CoFe<sub>2</sub>O<sub>4</sub> nanoparticles .....</b>	20
3.1. Introduction.....	20
3.2. Experimental section.....	21

3.2.1. Materials.....	21
3.2.2. Synthesis of CoFe <sub>2</sub> O <sub>4</sub> nanoparticles.....	21
3.2.3. Synthesis of Fe <sub>3</sub> O <sub>4</sub> nanoparticles.....	22
3.2.4. Characterization.....	23
3.3. Results and discussion.....	23
3.4. Conclusions.....	33
<b>IV. The synthesis of FePt and FePt/Fe<sub>3</sub>O<sub>4</sub> nanoparticles .....</b>	<b>34</b>
4.1. Introduction.....	34
4.2. Experimental section.....	36
4.2.1. Materials.....	36
4.2.2. Synthesis of FePt using thermal decomposition method.....	37
4.2.3. Cell culture and Cell viability.....	37
4.2.4. Characterization.....	39
4.3. Results and discussion.....	39
4.4. Conclusions.....	49
<b>References.....</b>	<b>50</b>
<b>Summary.....</b>	<b>55</b>

## List of Figures

- Figure 2-1. Crystal structure of cubic inverse spinel  $\text{Fe}_3\text{O}_4$ .
- Figure 2-2. Energy diagram of magnetic nanoparticles with different magnetic spin alignment, showing ferromagnetism in a large particle (top) and superparamagnetism in a small nanoparticle (bottom).
- Figure 2-3. Variation of intrinsic coercivity ( $H_{ci}$ ) with particle diameter  $D$ .
- Figure 2-4. Schematic drawing of the experiment equipment.
- Figure 2-5. Formation of Nanoparticles depending on time.
- Figure 3-1. TEM images of  $\text{CoFe}_2\text{O}_4$  nanoparticles with different shapes (a) Sphere shape, (b) Cube shape and (c, d) Hexagonal shape. The inset is a statistical analysis of the nanoparticles including average particles size (APS) and the standard deviations
- Figure 3-2. TEM images of  $\text{Fe}_3\text{O}_4$ nanoparticles with different shapes (a, b) Cube shape and (c, d) Hexagonal shape.
- Figure 3-3. TEM and HRTEM images of  $\text{Fe}_3\text{O}_4$  nanocubes
- Figure 3-4. Schematic diagram of morphological evolution of  $\text{CoFe}_2\text{O}_4$  NPs under different synthetic conditions (a) In case of this study and (b) In case of other reported works (Ref 13, 15, and 16)
- Figure 3-5. EDS elemental analysis of (a)  $\text{CoFe}_2\text{O}_4$  NPs and (b)  $\text{Fe}_3\text{O}_4$  NPs
- Figure 3-6. X-ray diffraction patterns of samples of (a)  $\text{CoFe}_2\text{O}_4$  nanosphere, (b)  $\text{CoFe}_2\text{O}_4$  nanocubes and (c)  $\text{CoFe}_2\text{O}_4$  nanohexagonal.
- Figure 3-7. X-ray diffraction patterns of samples of (a)  $\text{Fe}_3\text{O}_4$  nanocubes, (b)  $\text{Fe}_3\text{O}_4$  nanohexagonal.
- Figure 3-8. Hysteresis loops of  $\text{CoFe}_2\text{O}_4$  nanoparticles measured using SQUID at 300 K and a photograph of  $\text{CoFe}_2\text{O}_4$  NPs in solution in the absence and presence of an external magnet.
- Figure 3-9. Hysteresis loops of  $\text{Fe}_3\text{O}_4$  nanoparticles measured using SQUID at 300 K and a photograph of  $\text{Fe}_3\text{O}_4$  NPs in solution in the absence and presence of an external magnet
- Figure 4-1. Schematic of  $\text{FePt}$  nanoparticles formation from decomposition of  $\text{Fe}(\text{CO})_5$  and reduction of  $\text{Pt}(\text{acac})_2$  .
- Figure 4-2 Variation in iron composition ratio of  $\text{FePt}$  nanoparticles with different precursor

ratio.

- Figure 4-3. TEM images and Size distribution of FePt nanoparticles with different precursor ratio.  $\text{Fe}(\text{CO})_5 : \text{Pt}(\text{acac})_3 =$  ① 1 : 1, ② 2 : 1, ③ 3: 1, ④ 4: 1, ⑤ HRTEM of a single FePt nanocube, ⑥HRTEM of FePt/Fe<sub>3</sub>O<sub>4</sub> heterostructure.
- Figure 4-4. The EDS mapping images of synthesized homogeneous FePt nanoparticle using 1-octadecene.
- Figure 4-5. The EDS mapping images of synthesized heterodimer structure FePt/Fe<sub>3</sub>O<sub>4</sub> using 1-octadecene.
- Figure 4-6. Figure 4-6. The EDS elemental analysis of FePt nanoparticles
- Figure 4-7. Variation in iron composition ratio of FePt nanoparticles with different precursor ratio.
- Figure 4-8. TEM images and Size distribution of FePt nanoparticles with different precursor ratio.  $\text{Fe}(\text{CO})_5 : \text{Pt}(\text{acac})_3 =$  ① 1 : 1, ② 2 : 1, ③ 3: 1, ④ 4: 1
- Figure 4-9. The hysteresis loops of FePt nanoparticles with different precursor ratio at 300 K.
- Figure 4-10. The XRD patterns of FePt nanoparticles with different precursor ratio.
- Figure 4-11. The Cytotoxicity evaluated by 96 well assay in rage of 62.5 – 400  $\mu\text{g}/\text{ml}$  of FePt nanoparticles (A) 24 Hours, (B) 48 Hours.
- Figure 4-12. THP-1 Cells treated different concentration of FePt for 24 hours and stained with LIVE/DEAD staining solution.

## I . Introduction

Nanotechnology involves the study, control, and application of materials at the nanoscale, typically having dimensions less than 100 nm. The recent interest in nanostructures comes from their numerous potential applications such as biomedical sciences, electronics, optics, magnetism, energy storage, and electrochemistry. On the other hand, inorganic crystalline nanomaterials are of intense current interests because they often displayed unique and distinguished physical and chemical properties, which vary dramatically from those of their respective bulk forms [1-5].

Among the various types of nanomaterials, the magnetic nanoparticles (NPs) have been the subject of great interest because of its tremendous prospects in various potential applications including data storage, spintronics, sensor, environmental, energy and biology applications [6-15]. On the same time, the properties of nanoparticles are drastically altered by change of size and shape, making them ideal candidates for applications in catalysis, electronics, sensing, optics, solar cells, medical diagnostics, drug delivery, cellular signaling, nanomedicine, and so forth [16–19]. Therefore the morphology controlled of the nanoparticles in terms of shape and size of nanoparticles is very important for the various applications.

In sight of the diverse and widespread applications as well as the importance of magnetic nanoparticles morphology controlled, many groups have put efforts in synthesizing these materials using different methods, including sonochemical, sol-gel, polyol, co-precipitation, mechanochemical, microemulsion, hydrothermal, and thermal decomposition method.

Although all these approaches have succeeded to prepare magnetic nanoparticles with good properties, however, the extent of control over particle dispersion and morphology was not

adequate for achieving particles useful in real applications. In this thesis, we present a facile, safe, and convenient thermal decomposition route for morphology controlled synthesis of two kinds of ferrite of  $\text{Fe}_3\text{O}_4$  and  $\text{CoFe}_2\text{O}_4$  as well as one kind of magnetic alloy of FePt nanoparticles. Moreover, in our synthesis method, we avoids the using of complex procedures in terms of the needed to prepare an intermediate product such as iron oleate and or using excess amount of surfactants (e.g., 1,2-hexadecanediol, and octadecanol,1-octadecene etc.) which used in previous reports of thermal decomposition method[20-23]. Thus, simple modification of the reaction condition allowed us to obtain nanoparticles with various morphology including cubes, hexagons and spheres with wide size range distribution.

The overall goal of this thesis is to produce practically feasible various magnetic nanoparticles of oxide ( $\text{Fe}_3\text{O}_4$  and  $\text{CoFe}_2\text{O}_4$ ) and alloy (FePt) with various shapes and sizes for using in bio-applications. The principal objectives for achieving this goal are: (i) synthesis of  $\text{Fe}_3\text{O}_4$  ,  $\text{CoFe}_2\text{O}_4$  and FePt nanoparticles using a facile thermal decomposition method; (ii) functionalization of magnetic nanoparticles surfaces using inorganic materials capable of enhancing its stability, biocompatibility and surface binding affinity for bio-molecules as well as their dispersion properties, thus meeting the requirements of various practical applications; (iii) the use of functionalized magnetic nanoparticles in plasma treatment for bio-application.

The thesis-containing 4 chapters are organized as follows :

In **Chapter 1**, a general introduction about the importance of nanoparticles and especially the magnetic nanoparticles are described with explanation of the materials which synthesized and also the method which we used.

In **Chapter-2**, the experimental tools (in this study) for the synthesis of magnetic ferrites and alloy nanoparticles are outlined. The thermal decomposition method, apparatus and reaction mechanism are discussed in detail. In addition, the techniques that were used for the characterization of the magnetic nanoparticles are also briefly explained.

In **Chapter-3**, the synthesis of  $\text{Fe}_3\text{O}_4$  and  $\text{CoFe}_2\text{O}_4$  nanoparticles with various shapes and sizes using the thermal decomposition method is described in detail. The details of the mechanism for shape and size controlling of nanoparticles is described in details. Also, the characterization techniques which used are described, including X-ray diffraction (XRD), transmission electron microscopy (TEM), energy dispersive spectrometer (EDS), and Vibrating Sample Magnetometer (VSM).

In **Chapter-4**, the synthesis of FePt nanoparticles with various shapes and sizes using the thermal decomposition method is described in detail. The application of the synthesized FePt for the bio-application is explained.

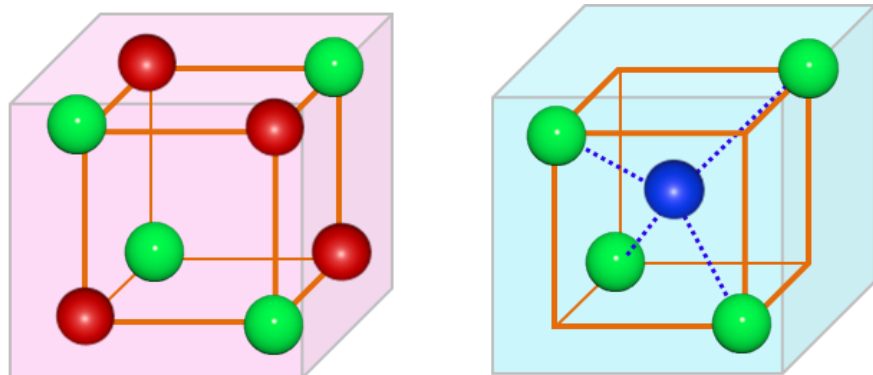
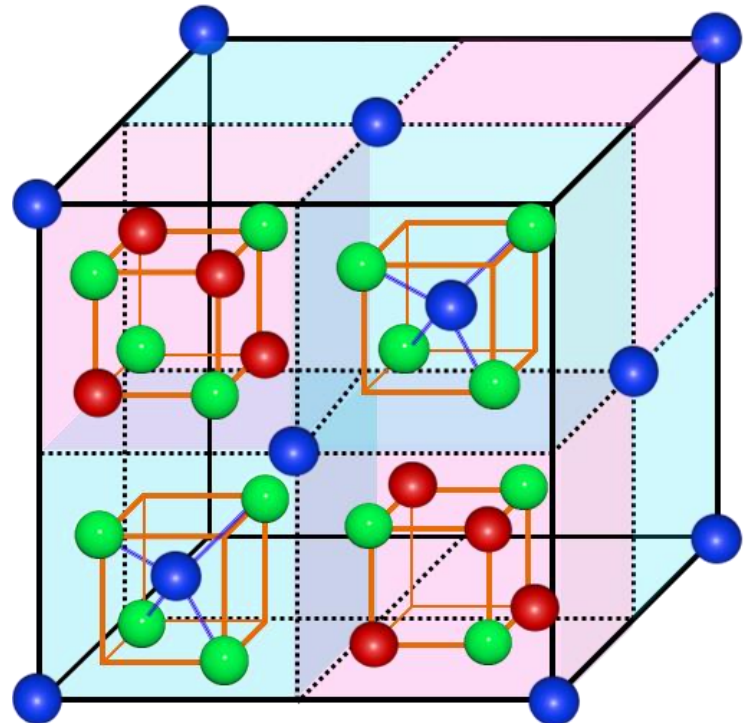
## II . Research background

### 2.1 Magnetic nanoparticles

#### 2.1.1 Ferrite

Among all kinds of iron oxides materials, magnetite with chemical formula of ( $\text{Fe}_3\text{O}_4$ ) possess the most interesting properties and has the highest saturation magnetization value among their magnetic oxide counterpart, like maghemite ( $\gamma\text{-Fe}_2\text{O}_3$ ), goethite ( $\alpha\text{-FeOOH}$ ) and hematite ( $\alpha\text{-Fe}_2\text{O}_3$ ). In general, magnetite ( $\text{Fe}_3\text{O}_4$ ) has a cubic inverse spinel structure with lattice constant of  $a = 0.839$ . In the unit cell, as shown in Fig. 2-1, the oxygen ions form an fcc closed packing, and the iron ions occupy interstitial tetrahedral sites and octahedral sites, symbolized as  $[\text{Fe}^{3+}]_A\text{-}[\text{Fe}^{2+}\text{Fe}^{3+}]_B\text{O}_4$ , in which  $A$  (tetrahedral positions) is occupied by  $\text{Fe}^{3+}$  ions and  $B$  (octahedral sites) is occupied by eight  $\text{Fe}^{2+}$  ions and eight  $\text{Fe}^{3+}$  ions. Magnetite is ferrimagnetic at room temperature and has a Curie temperature of 850 K. Nevertheless, the term ferromagnetic is generally used for magnetite nanoparticles, and the magnetic properties of  $\text{Fe}_3\text{O}_4$  are ascribed to the splitting of the 5d orbitals. The 5d orbitals are split into two subsets due to the oxide ligands and all  $\text{Fe}^{3+}$  and  $\text{Fe}^{2+}$  ions have four unpaired electrons, respectively.

In the octahedral site,  $\text{Fe}^{3+}$  and  $\text{Fe}^{2+}$  ions are coupled ferromagnetically through a double exchange mechanism, and the  $\text{Fe}^{3+}$  ions in tetrahedral and octahedral sites are coupled antiferromagnetically via the oxygen, implying that the  $\text{Fe}^{3+}$  spins cancel out each other and thus merely unpaired spins of  $\text{Fe}^{2+}$  in octahedral coordination contribute to the magnetization. And If the  $\text{Fe}^{2+}$  ions in some of the octahedral sites were oxidized, the saturation magnetization ( $M_s$ ) would decrease. [24, 26]



- Octahedral site  $\text{Fe}$  ion
- Tetrahedral site  $\text{Fe}$  ion
- $\text{O}^{2-}$  ion

Figure 2-1. Crystal structure of cubic inverse spinel  $\text{Fe}_3\text{O}_4$ .

## 2.1.2 Other types of ferrites

Alternatively other types of ferrites were also studied for biomedical applications. In these ferrites, as compared to the iron oxide nanocrystals,  $\text{Fe}^{2+}$  ions are fully or partially replaced by other transition metals in spinel structure and they represented by a general formula ( $M\text{Fe}_2\text{O}_4$ ;  $M=\text{Zn, Ni, Co, Mn}$ ). Manganese ferrites ( $\text{MnFe}_2\text{O}_4$ ) serve as potential MRI contrast agents with largest magnetization among other ferrites and zinc ferrite ( $\text{ZnFe}_2\text{O}_4$ ) nanocrystals demonstrated better MRI contrast with respect to similar magnetite nanocrystals. On the other side as regard to magnetic hyperthermia, the use of cobalt ferrites ( $\text{CoFe}_2\text{O}_4$ ), known by its high magnetic anisotropy energy which is responsible for holding the magnetization along certain direction, has proven to be a good way since much higher heating rates were reported for these nanocrystals compared to other ferrites. Another strategy followed in the design of magnetic core for biomedical applications is the synthesis of mixed ferrites, where simple ferrites including one kind of magnetic ion except iron are doped with other kind of magnetic ion. This is generally realized in order to utilize from different outstanding magnetic features of different ions. For example in hyperthermia application, Co, being a hard magnetic material, is doped to other ferrites ( $M\text{Fe}_2\text{O}_4$ ) in changing concentrations ( $\text{Co}_x\text{M}_{1-x}\text{Fe}_2\text{O}_4$ ;  $x=\text{concentration}$ ) in order to increase the magnetic anisotropy eventually to improve the heat transfer rate, whereas Zn is added for reducing the Curie temperature of resulting mixed ferrite. This latter operation permits the tuning of the maximum reached temperature by heat transfer and prohibits overheating of healthy tissues via the process called self-controlled hyperthermia. Table. 2-1 summarizes some important magnetic parameters of transition metal oxides (ferrites) used in biomedical applications.

Ferrites	RT saturation magnetization M <sub>s</sub> (emu/g)	Anisotropy constant K <sub>1</sub> (x10 <sup>4</sup> J/m <sup>3</sup> )	Curie temperature T <sub>c</sub> (°C)	Superpara magnetic size D <sub>SP</sub> (nm)
Fe <sub>3</sub> O <sub>4</sub>	90-100	-1.2	585	25
NiFe <sub>2</sub> O <sub>4</sub>	56	-0.68	585	28
CoFe <sub>2</sub> O <sub>4</sub>	80-94	18-39	520	14
MnFe <sub>2</sub> O <sub>4</sub>	80	-0.25	300	25

Table 2-1. Magnetic parameters (saturation magnetization, first degree anisotropy constant, Curie temperature and superparamagnetic transition size at RT) of ferrites. [24]

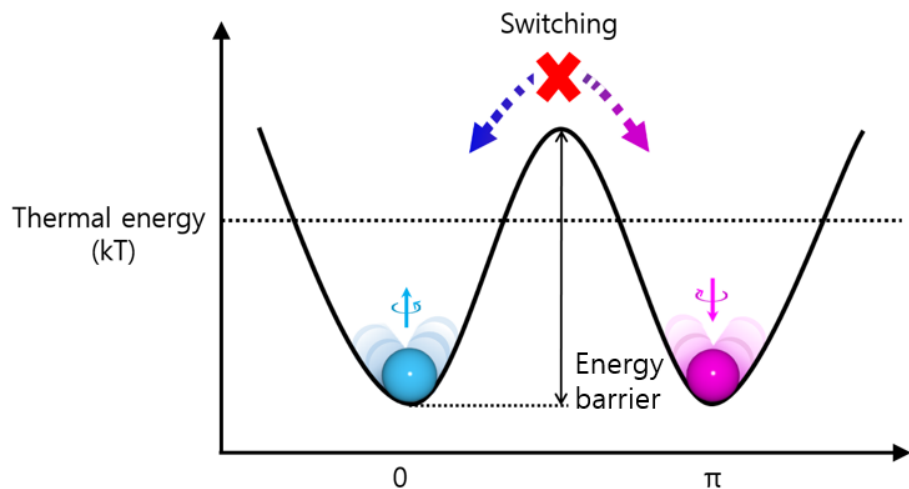
Another class of materials used as magnetic cores are the magnetic alloy nanoparticles, which composed of two or three different kind of metals like FeCo, FePt and NiCu. FePt is the most famous one among these materials due to its chemical stability and high magnetic anisotropy. Maenosono and Saita have studied FePt nanocrystals and proposed them to be used as high performance contrast agents and heating mediators in MRI and magnetic hyperthermia, respectively. [24]

## 2.2 Magnetic properties

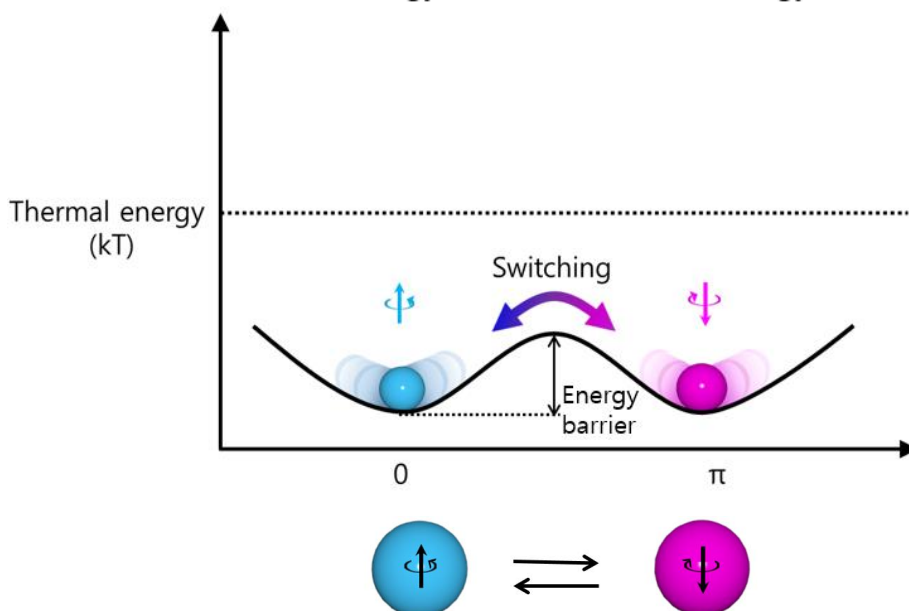
### 2.2.1 Superparamagnetism

The magnetic anisotropic energy barrier from a spin-up state to spin-down state of the magnet is proportional to the product of the magnetic anisotropic constant ( $K_u$ ) and the volume ( $V$ ) of the magnet. While bulk materials have magnetic anisotropic energies that are much larger than the thermal energy ( $kT$ ) (blue line in figure 2-2. below), the thermal energy of the nanoparticle is sufficient to readily invert the magnetic spin direction, although it is insufficient to overcome the spin-spin exchange coupling energy (red line). Such magnetic fluctuation leads to a net magnetization of zero, and this behavior is called superparamagnetism. [28]

Consequently, the collective behavior of the magnetic nanoparticles is the same as that of paramagnetic atoms. Although the magnetic order still exists in the nanoparticles, each particle behaves like a paramagnetic atom but with a giant magnetic moment. When a superparamagnetic state is achieved, the magnetic nanoparticle goes through a superparamagnetic relaxation process, in which the magnetization direction of the nanoparticle rapidly fluctuates instead of fixing along a certain direction. The temperature, at which the magnetic anisotropy energy barrier of a nanoparticle is overcome by thermal activation and the nanoparticle becomes superparamagnetically relaxed, is known as the blocking temperature. Below the blocking temperature, thermal fluctuations are not large enough to reverse the magnetization and an irreversible magnetization curve is observed. Determination of the blocking temperature can be measured by SQUID magnetometer. [27]



Large nanoparticles : Ferromagnetism  
Energy barrier > Thermal energy



Small nanoparticles : Superparamagnetism  
Energy barrier < Thermal energy  
"Spin fluctuation"

Figure 2-2. Energy diagram of magnetic nanoparticles with different magnetic spin alignment, showing ferromagnetism in a large particle (top) and superparamagnetism in a small nanoparticle (bottom).

The temperature-dependent magnetization M (T) exhibits a cusp in the zero field-cooled (ZFC) susceptibility at the blocking temperature, Tb. Above Tb, the particles are free to align with the field during measurement. The magnetization of a system of particles, M, is described by the Langevin function. [25]

$$\frac{M}{M_S} = L\left(\frac{\mu H}{k_B T}\right) = \coth\left(\frac{\mu H}{k_B T}\right) - \frac{k_B T}{\mu H} \quad (2-1)$$

where  $\mu (=M_S\pi D^3 / 6)$  is the magnetic moment of a single particle and  $M_S$  is the saturation magnetization. At low fields ( $\mu H \ll k_B T$ ), the magnetization behaves as  $\mu H/3k_B T$  and at high fields ( $\mu H \gg k_B T$ ), as  $1-k_B T/\mu H$ . If a distribution of particle sizes is present, the initial susceptibility is sensitive to the larger particles present, and the approach to saturation is more sensitive to the smaller particles present.

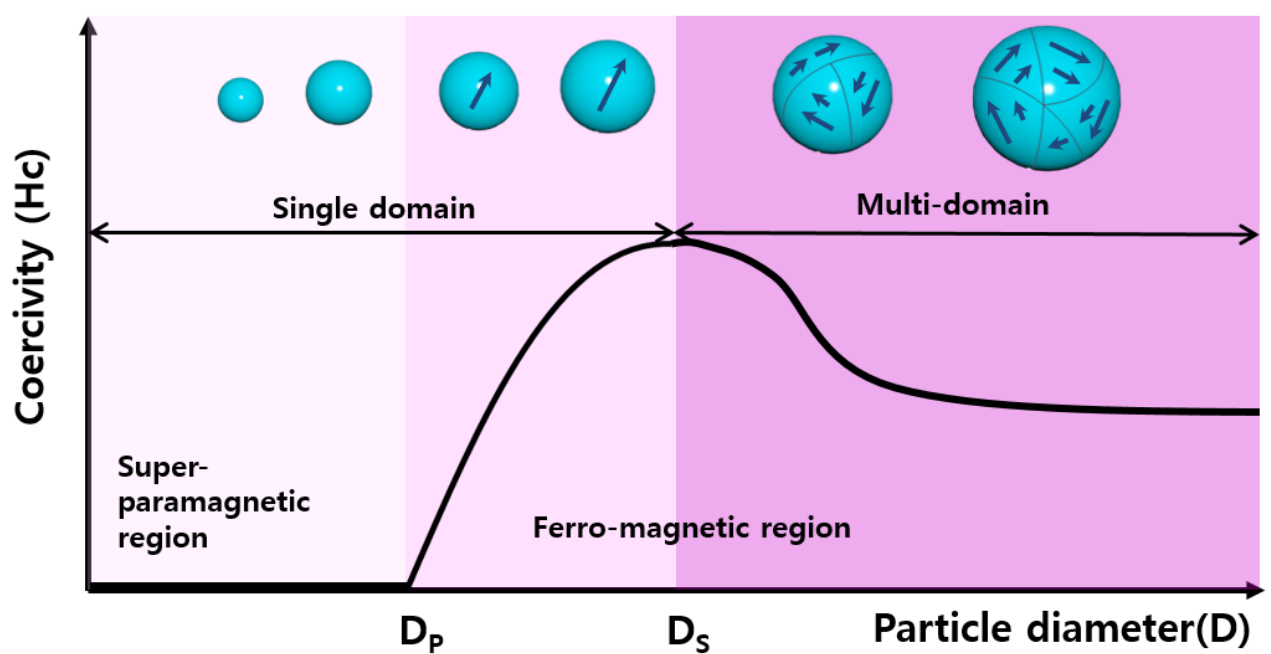


Figure 2-3. Variation of intrinsic coercivity ( $H_{ci}$ ) with particle diameter  $D$ . [29]

## 2.2.2 Anisotropy

Anisotropy of materials affects the magnetic behaviors in most cases. The most common classifications of anisotropy are i) crystal anisotropy, ii) shape anisotropy, iii) stress anisotropy, iv) externally induced interaction anisotropy, and v) exchange anisotropy. The anisotropy (EA) can often be modeled as uniaxial in character and represented by  $EA = KV \sin^2 \theta$  (2.7) Where K is the effective uniaxial magnetocrystalline anisotropy constant per unit volume,  $\theta$  is the angle between the magnetization direction and the easy axis of nanoparticle, and V is the volume of the nanoparticle. For magnetic nanoparticles with a spherical shape, magnetocrystalline anisotropy can be approximated as the total magnetic anisotropy. This anisotropy acts as an energy barrier to prevent the change of magnetization direction. Magnetocrystalline anisotropy arises from spin-orbit coupling and energetically favors alignment of the magnetization along a specific crystallographic direction. The magnetocrystalline anisotropy is specific to a given material and independent of particle shape. In hcp cobalt as an example, magnetocrystalline anisotropy causes the magnetization to point along the c axis. In the cubic systems, (such as Fe and Ni) symmetry creates multiple easy axes. In nickel, the axes are the easy axes, while the axes are the easy axes in iron. The magnitude of the magnetocrystalline anisotropy at a room temperature is  $7 \times 10^6$  erg/cm<sup>3</sup> in Co,  $8 \times 10^5$  erg/cm<sup>3</sup> in Fe, and  $5 \times 10^4$  erg/cm<sup>3</sup> in Ni. The coercivity is proportional to the anisotropy constant, so high anisotropy materials (such as rare-earth cobalt, which have anisotropy approaching 108 erg/cm<sup>3</sup>) are considered as attractive candidates for high coercivity applications. [27]

## **2.3 Synthesis method of magnetic nanoparticles**

### **2.3.1 Co-Precipitation**

The most conventional method for obtaining  $\text{Fe}_3\text{O}_4$  is by co-precipitation. This method consists of mixing ferric and ferrous ions in a 1:2 molar ratio in highly basic solutions at room temperature or at elevated temperature. The size and shape of the iron oxide NPs depends on the type of salt used, the ferric and ferrous ions ratio, the reaction temperature, the PH value, ionic strength of the media, and the other reaction parameters. Recently we have reported the co-precipitation synthesis of  $\text{Fe}_3\text{O}_4$  NPs and their corresponding morphology, structure, and magnetic properties at different reaction temperature was investigated. This method would critically affect the physical and chemical properties of the nanosized iron oxide particles. Generally, the saturation magnetization ( $M_s$ ) values found in nanostructured materials are usually smaller than the corresponding bulk phase, provided that no change in ionic configurations occurs. Accordingly, experimental value for  $M_s$  in magnetic iron oxide NPs have been reported to span the 30–80 emu g<sup>-1</sup> range, lower than the bulk magnetic value 100 emu g<sup>-1</sup>. In addition,  $\text{Fe}_3\text{O}_4$  NPs are not very stable under ambient conditions and are easily oxidized to  $\text{Fe}_2\text{O}_3$  or dissolved in an acidic medium. In order to avoid the possible oxidation in the air, the synthesis of  $\text{Fe}_3\text{O}_4$  NPs must be done in an anaerobic conditions. Based on this point,  $\text{Fe}_3\text{O}_4$  NPs can also be utilized to prepare the  $\text{Fe}_2\text{O}_3$  NPs by oxidation or anneal treatment under oxygen atmosphere. And oxidation is not the important influence factor for  $\text{Fe}_2\text{O}_3$  NPs due to its own chemical stability in alkaline or acidic environment.

However, this method generates particles with a wide particle size distribution, which requires secondary size selection sometimes. A wide particle size distribution will result in a wide range of blocking temperatures ( $T_B$ ) due to  $T_B$  depends on particle size and, therefore

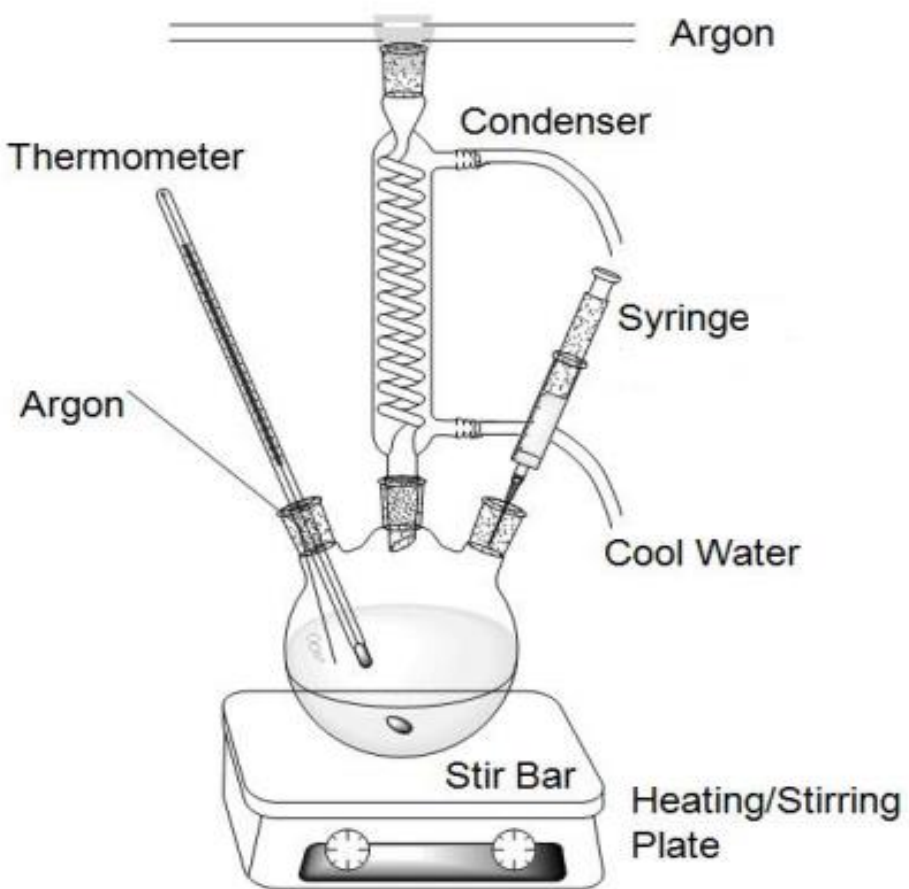


Figure 2-4. Schematic drawing of the experiment equipment. [30]

non-ideal magnetic behavior for many applications. Kang et al. reported a synthesis of monodispersed, uniform, and narrow size distributional Fe<sub>3</sub>O<sub>4</sub> NPs (the diameter of NPs was  $8.5 \pm 1.3$  nm) by co-precipitation without surfactants, the reaction in an aqueous solution with a molar ratio of Fe<sup>II</sup>/Fe<sup>III</sup> = 0.5 and a pH = 11–12, and the colloidal suspensions of the magnetite can be then directly oxidized by aeration to form colloidal suspensions of  $\gamma$ -Fe<sub>2</sub>O<sub>3</sub>. In contrast, many recent publications have described efficient routes to obtain the monodispersed NPs, surfactants such as dextran or polyvinyl alcohol (PVA) can be added in the reaction media, or the particles can be coated in a subsequent step. Surfactants act as protecting agent for controlling particle size and stabilizing the colloidal dispersions.

Additionally, the disadvantage of these aqueous solution syntheses is that the high pH value of the reaction mixture has to be adjusted in both the synthesis and purification steps, and the process toward uniformed and monodispersed NPs has only very limited success. On the other hand, wastewaters with very basic pH values are also generated in the experiment, which require subsequent treatments for protecting the environment.[31]

### **2.3.2 Thermal decomposition**

An organic solution phase decomposition route has been widely used in iron oxide NPs synthesis, and decomposition of Fe(cup)<sub>3</sub>(cup = *N*-nitrosophenylhydroxylamine), Fe(acac)<sub>3</sub> (acac = acetylacetone), or Fe(CO)<sub>5</sub> followed by oxidation can lead to high-quality monodispersed iron oxide NPs, which usually requires relatively higher temperatures and a complicated operation.

Generally, direct decomposition of Fe(Cup)<sub>3</sub> single precursor can lead to monodispersed  $\gamma$ -Fe<sub>2</sub>O<sub>3</sub> nanoparticles. The thermal decomposition of Fe(CO)<sub>5</sub> produces iron NPs and the

following oxidation by a chemical reagent can also lead to monodispersed  $\gamma$ -Fe<sub>2</sub>O<sub>3</sub> nanoparticles. Although the thermal decomposition method has many advantages for producing highly monodispersed particles with a narrow size distribution, it has the big disadvantage that the resulting NPs are generally only dissolved in nonpolar solvents. [31]

### **2.3.3 Formation of nanoparticles**

The particle formation process is classified into the prenucleation, nucleation, and growth stages. The monomer concentration increases with time (prenucleation). When the precursor monomer concentration reaches a critical value, generation of nucleus begins (nucleation stage).

The smallest diameter of stable nuleus is determined by the free energy of the aggregation of nuclei and the surface area. Then, monomers supplied are consumed for the growth of the stable nuclei (growth stage). To synthesize a monodispersed particle, it is desirable to separate the nucleation and the growth stages. However, in general, it is difficult to separate stage. Consequently, the supplied monomers are consumed competitively by the nucleation and the growth of the generated nuclei. Therefore, to synthesize monodispersed particles, we have to increase the nucleation rate or decrease the growth rate as much as possible. It is necessary to know the change in the supersaturation ratio and the aggregation of nuclei with time. It is possible to obtain the situation in which the growth of seed only occurs if the monomer concentration is kept constant between the saturation and the supersaturation monomer concentrations by adding seeds to the system. The crystallinity (crystalline or amorphous) and the type of particle growth are also important. Furthermore, the reaction temperature, raw material concentration, coexistence of ion species, and solution pH, etc., which are directly related to the controlling factors, are very important. [32]

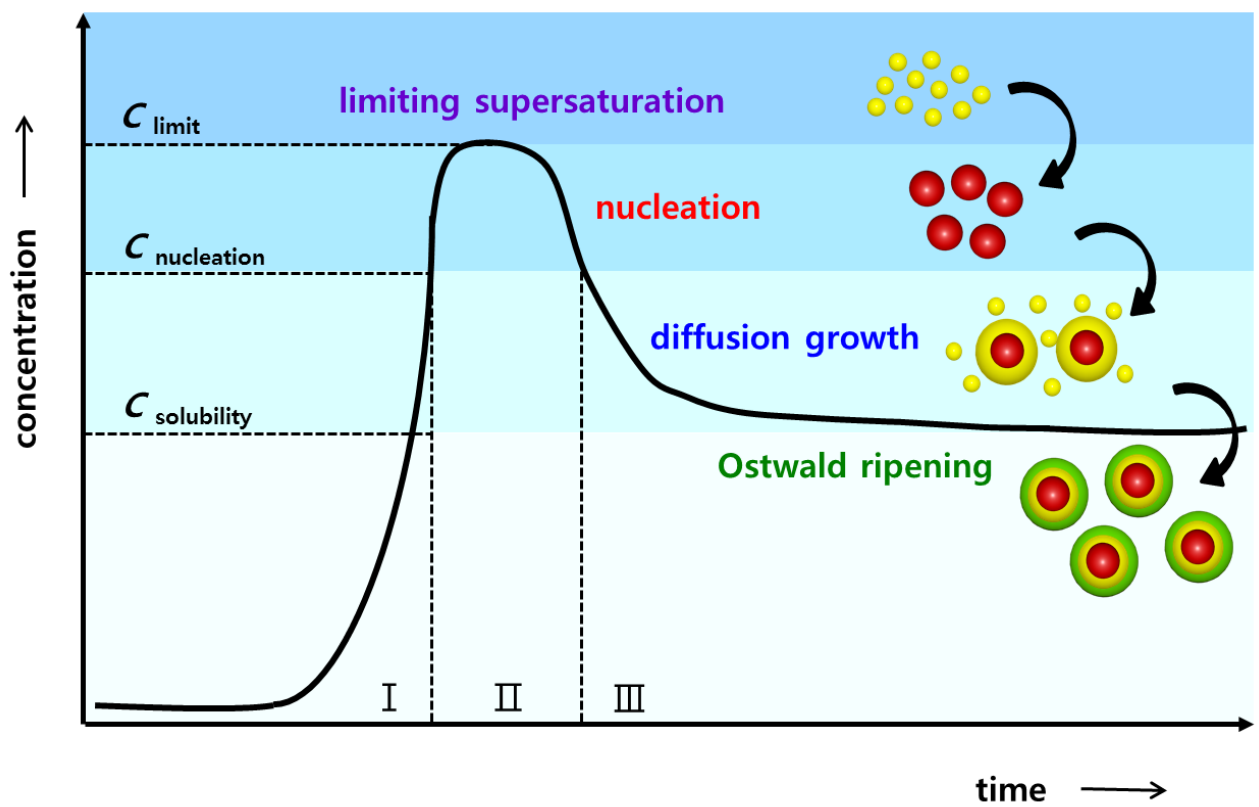


Figure 2-5. Formation of Nanoparticles depending on time. [33]

## **2.4 Characterization**

### **2.4.1 Transmission Electron Microscopy**

The size and morphology of the nanoparticles were characterized using transmission electron microscopy (TEM, Hitachi HF-3300). The chemical composition was analyzed by the EDS detector embedded on the TEM. The TEM principles are similar with light microscope but TEM has electrons beam which is much smaller wavelength than light so could be focused images with much better resolution. Samples for TEM analysis are prepared by depositing one drop of dilute nanoparticles dispersion in solvents such as hexane, ethanol, chloroform, water on amorphous carbon coated copper grids.

### **2.4.2. X-ray diffraction**

X-ray diffraction is used to obtain the crystal structure information of magnetic nanoparticles. From XRD pattern, we can get many information including reflection planes, lattice parameter and crystallite size of the sample using Scherrer equation and so on. Diffraction occurs with the result of interaction of radiation with atom's electron and can explain with Bragg's law. [34]

$$n\lambda = 2d \sin \theta \quad (2-2)$$

Where  $\lambda$  is the wavelength of the beam (Cu K $\alpha$  radiation  $\lambda=1.540562 \text{ \AA}$ ), n is integer,  $\theta$  is the half value of the peak position and d is the spacing of diffraction plane.

And the crystallite size of the sample was calculated from the XRD pattern using the Scherrer equation. [34]

$$D = K \lambda / \beta \cos \Theta \quad (2-3)$$

Where  $\lambda$  is the wavelength of the beam (1.540562 Å),  $\beta$  is the full width at half maximum (FWHM),  $\theta$  is the Bragg angle for the studied peak/ring, and  $K$  is the shape factor.

#### **2.4.3 Vibrating Sample Magnetometer.**

Vibrating Sample Magnetometer (VSM) measure magnetic moment of a sample with good precision. A sample is loaded at the end of rod and vibrated with a fixed frequency and vertical direction by oscillator (~80Hz). A horizontal magnetic field from electromagnet make a sample magnetized. And a vibrated sample's magnetic moment change the magnetic flux through search coil. The search coil sense induced electromotive force of a vibrated sample which is based faraday's law of induction. VSM (Lake Shore Magnetometers, 7407) has sensitivity at room temperature around  $0.1 \sim 0.4 \mu\text{emu}$  and maximum field at room temperature around 3.05 T. [35]

### **III. The synthesis of Fe<sub>3</sub>O<sub>4</sub> and CoFe<sub>2</sub>O<sub>4</sub> nanoparticles**

#### **3.1 Introduction**

Magnetic nanoparticles (MNPs) have been studied extensively within the last decade and till now in part due to their diverse potential for application in biomedicine, catalysis, electronic and energy fields.[36-38] Ferrites nanoparticles (NPs) in particular have been comprehensively investigated for a variety of applications due to their unique magnetic properties, high electrical resistivity, mechanical properties, and high chemical stability.[39,40] However, the potential application of MNPs in a number of fields will depend on the ability to produce materials with high crystallinity, stability, dispersion, and magnetic behavior. Notably, NP has a tremendous impact on resulting properties and potential applications. Indeed, changing the crystal shape of nanoparticles alters the exposed crystal facets and hence atomic arrangements in each facet which will have significant effect on its various properties. [41]

Various approaches including sonochemical, polyol, and hydrothermal synthesis, microemulsion, thermal decomposition, and co-precipitation have been used to target ferrite NPs with various sizes and morphologies.[42-46] Among these methods, thermal decomposition is considered the most attractive approach for accessing ferrite NPs with high crystallinity and uniform particle size distribution.

In our previous work, we used the sonochemical technique to synthesize Fe<sub>3</sub>O<sub>4</sub> and CoFe<sub>2</sub>O<sub>4</sub> nanoparticles with high crystallinity and large magnetic moment[47], however, the extent of control over particle dispersion and morphology was not adequate for achieving particles useful in real applications. In this paper, we present a facile, safe, and convenient thermal decomposition route for morphology controlled synthesis of two kinds of ferrite of Fe<sub>3</sub>O<sub>4</sub> and CoFe<sub>2</sub>O<sub>4</sub>. Moreover, in our synthesis approach, we avoids the using of complex procedures in

terms of the needed to prepare an intermediate product such as iron oleate and or using excess amount of surfactants (e.g, 1,2-hexadecanediol, and octadecanol, 1-octadecene, etc.) which used in previous reports of thermal decomposition method.[45-50] Thus, simple modification of the reaction condition allowed us to isolate nanoparticles as cubes, hexagons and spheres with sizes ranging from 5 to 150 nm. Oleic acid and oleylamine were used as the solvents, stabilizers, and reducing agents[51] and iron(III) acetylacetone and cobalt(II) acetylacetone were successfully employed as precursors instead of commonly used toxic, flammable and expensive pentacarbonyl.[52,53] The  $\text{Fe}_3\text{O}_4$  and  $\text{CoFe}_2\text{O}_4$  nanoparticle morphology, composition and crystalline structure were monitored using X-ray diffraction (XRD), transmission electron microscope (TEM), high resolution transmission electron microscopy (HRTEM), energy dispersive spectroscopy (EDS) and their magnetic properties were characterized using superconducting quantum interference device (SQUID) from -15 kOe to +15 kOe at 300K.

## **3.2 Experimental section**

### **3.2.1 Materials**

Iron(III) acetylacetone (97%), cobalt( II ) acetylacetone (98%), benzyl ether (98%), oleic acid (99%), oleylamine (98%) were purchased from Sigma-Aldrich, Ltd. All of the chemicals were of analytical reagent grade and used as received without any further purification.

### **3.2.2 Synthesis of $\text{CoFe}_2\text{O}_4$ nanoparticles**

Three shapes of sphere, cube, and hexagonal of  $\text{CoFe}_2\text{O}_4$  NPs were synthesized using thermal decomposition method. Firstly, for synthesis of  $\text{CoFe}_2\text{O}_4$  nanosphere, suitable amount of Iron (III) acetylacetone and cobalt( II ) acetylacetone were dispersed in 40 ml benzyl

ether as solvent media in three neck round-bottom flask using mechanical stirrer. After that, 3 mL of each oleic acid and oleylamine were added simultaneously to the above solution. The mixture was heated to 100 °C with a heating rate of 10 °C min<sup>-1</sup> and kept for 60 min at this temperature. Thereafter, the reaction temperature was increased to 290 °C with a heating rate of 10 °C min<sup>-1</sup> and kept refluxing for 45 min. The mixture was cooled down to room temperature naturally and then collected the precipitate using a permanent magnet. The collected CoFe<sub>2</sub>O<sub>4</sub> nanoparticles were washed using a mixture solvent of acetone and ethanol at room temperature to remove any impurities. The washing process repeated for five times and in every time the magnetic nanoparticles were collected using a permanent magnet.

For the synthesis of CoFe<sub>2</sub>O<sub>4</sub> nanocubes, we used the same procedures mentioned above with decreasing the amount of benzyl ether to 20 mL and using only oleic acid (2.5 ml) as reducing agent with reducing the reaction time to be 30 min at 290 °C. For synthesis of hexagonal shape of CoFe<sub>2</sub>O<sub>4</sub> NPs, we further decreasing the amount of benzyl ether to 15 ml and increasing the reaction time to 90 min at 290 °C.

### **3.2.3 Synthesis of Fe<sub>3</sub>O<sub>4</sub> nanoparticles**

Fe<sub>3</sub>O<sub>4</sub> nanoparticles with two different shapes of nanocubes and nanohexagonal were also synthesized using the same procedures used in case of CoFe<sub>2</sub>O<sub>4</sub> NPs of thermal decomposition method. For a typical synthesis of Fe<sub>3</sub>O<sub>4</sub> nanocubes, 3 mmol of Iron (III) acetylacetone was mixed with 15 mL benzyl ether and 3 mL oleic acid using mechanical stirring in three neck round-bottom flask. The mixture was heated to 100 °C with a heating rate of 10 °C min<sup>-1</sup> and kept at this temperature for 60 min, and then the temperature increased to 260 °C with refluxing for 90 min. The mixture was cooled down to room temperature naturally and then we collected the precipitate using a permanent magnet. The collected Fe<sub>3</sub>O<sub>4</sub> nanocubes were washed using

a mixture solvent of acetone and ethanol at room temperature to remove any impurities. The washing process repeated for five times and in every time the magnetic nanoparticles were collected using a permanent magnet. For synthesis of  $\text{Fe}_3\text{O}_4$  nanohexagonal, we used the same procedures mentioned above exactly with increasing only the temperature up to 290 °C.

### 3.2.4 Characterization

The crystal structures of the as-synthesized  $\text{CoFe}_2\text{O}_4$  and  $\text{Fe}_3\text{O}_4$  nanoparticles were analyzed using X-ray powder diffraction (XRD, Rigaku D/max-250) with Cu K $\alpha$  radiation ( $\lambda=1.540562 \text{ \AA}$ ) in the  $2\theta$  range from 20 to 80°. The morphology and size of the nanoparticles were characterized using transmission electron microscopy (TEM, The Tecnai G2 F20 operated at 300 kV) and high resolution transmission electron microscopy (HRTEM). And the chemical compositions of the nanoparticles were analyzed by an EDS analysis which coupled with the TEM equipment. The magnetic properties of the nanoparticles were measured by SQUID.

## 3.3 Results and discussion

A facile thermal decomposition route was designed in our study for producing different shapes and sizes of  $\text{Fe}_3\text{O}_4$  and  $\text{CoFe}_2\text{O}_4$  nanoparticles. Noteworthy, in the most of recently reported works for synthesis of ferrite NPs using thermal decomposition method, they used much amount of surfactant and reducing agent, like 1,2-hexadecanediol and octadecanol, *N* – nitrosophenylhydroxylamine, etc,<sup>13</sup> and or complicated procedure including the synthesis of iron oleate complex as intermediate then thermal decomposition.[48] Indeed, several studies have reported that controlling the nucleation and growth dynamics by modifying the heating rate, temperature, and the precursor concentration can result in the formation of various shaped

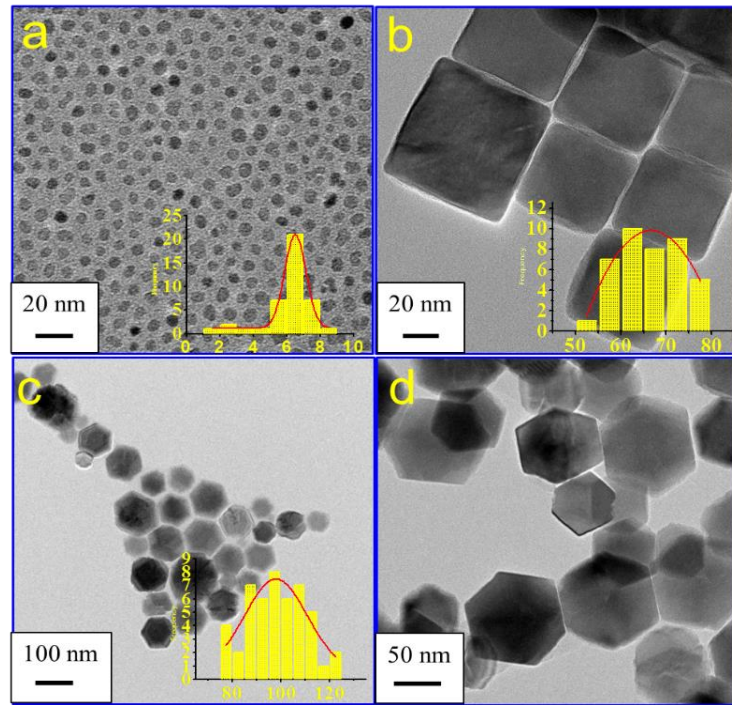


Figure 3-1. TEM images of  $\text{CoFe}_2\text{O}_4$  nanoparticles with different shapes (a) Sphere shape, (b) Cube shape and (c, d) Hexagonal shape. The inset is a statistical analysis of the nanoparticles including average particles size (APS) and the standard deviations

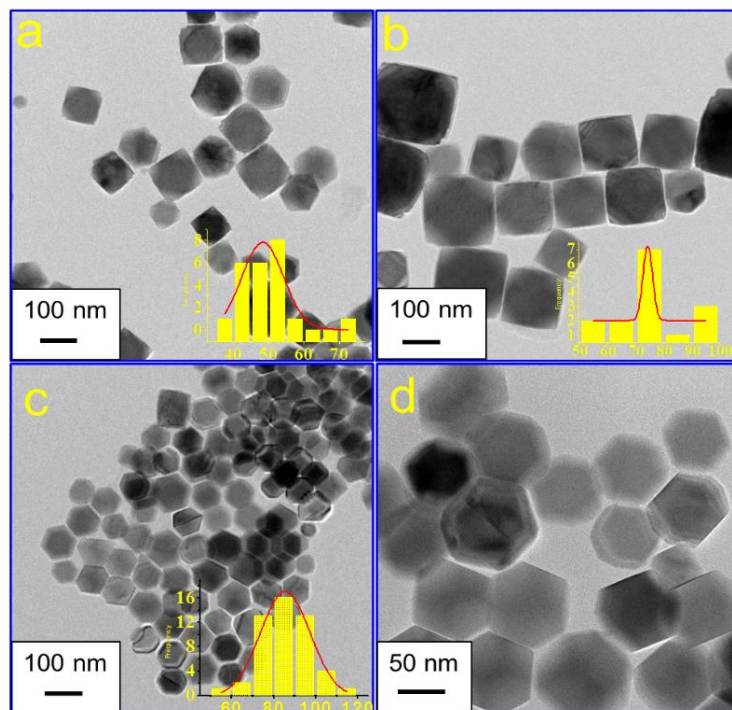


Figure 3-2. TEM images of  $\text{Fe}_3\text{O}_4$  nanoparticles with different shapes (a, b) Cube shape and (c, d) Hexagonal shape.

nanocrystals. [54] However, in this study, the morphology controlled of the nanoparticles was successfully achieved through the modification of reaction parameters, includes reaction temperature and the amount of benzyl ether as a solvent.

The morphology of the as-synthesized  $\text{CoFe}_2\text{O}_4$  and  $\text{Fe}_3\text{O}_4$  nanoparticles was investigated using transmission electron microscopy. A statistical analysis has been done for each sample of  $\text{CoFe}_2\text{O}_4$  and  $\text{Fe}_3\text{O}_4$  nanoparticles through counting some particles, and the average size is estimated from TEM micrograph using the lognormal distribution (see inset of Fig. 1 and 2). Fig. 1 shows different TEM images of  $\text{CoFe}_2\text{O}_4$  nanoparticles with various shapes. Monodisperse sphere-like shapes of 6.5 nm size of  $\text{CoFe}_2\text{O}_4$  nanoparticle were obtained when we used 40 mL of benzyl ether and 3 mL of each oleic acid and oleylamine for 45 min of refluxing time (Fig. 1a). However, highly crystalline nanocube with average particles size of 66.6 nm were produced when the amount of solvent was decreased to 20 mL while using oleic acid as a sole reducing agent at 30 min refluxing time (Fig. 1b). Interestingly, further decreasing of the solvent amount to 15 mL and increasing the reaction time to 90 min resulted in evolution of the nanocubes shape to be hexagonal with medium particle size of 98 nm (Fig. 1 c, d). The shape evolution of the nanoparticles in our study is mainly ascribed to the crucial role of the surfactant and reaction time. Hence, increasing the ratio of surfactant to solvent and also prolonging the reaction time at 260 °C to 90 min, not only does the {111} surface show saturated surface coverage, the surface {100} is also coordinated by the capping ligand, resulting in hexagon shapes with both {100} and {111} surfaces well developed.<sup>21</sup> Fig. 2 shows the TEM images of the as-synthesized  $\text{Fe}_3\text{O}_4$  nanoparticles with two different shapes of cubic and hexagonal. Fig. 2a shows TEM images of  $\text{Fe}_3\text{O}_4$  nanocubes with average particles size distribution of 48.4 nm obtained at 260 °C refluxing temperature and 90 min of reaction time. On the same time, when we prolonged the time of reaction to 120 min, the size of the nanocubes increased to be 74.5 nm (Fig. 2 b). However, increasing the reaction temperature to 290 °C,

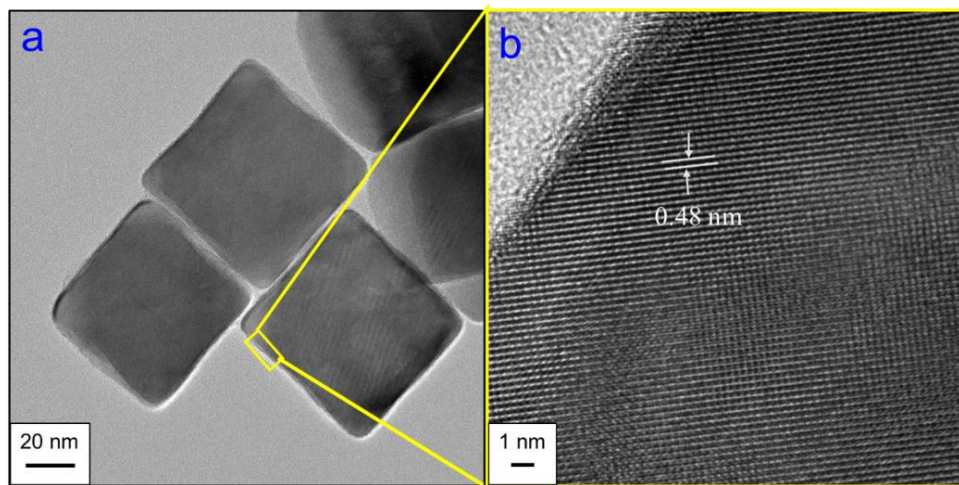


Figure 3-3. TEM and HRTEM images of  $\text{Fe}_3\text{O}_4$  nanocubes.

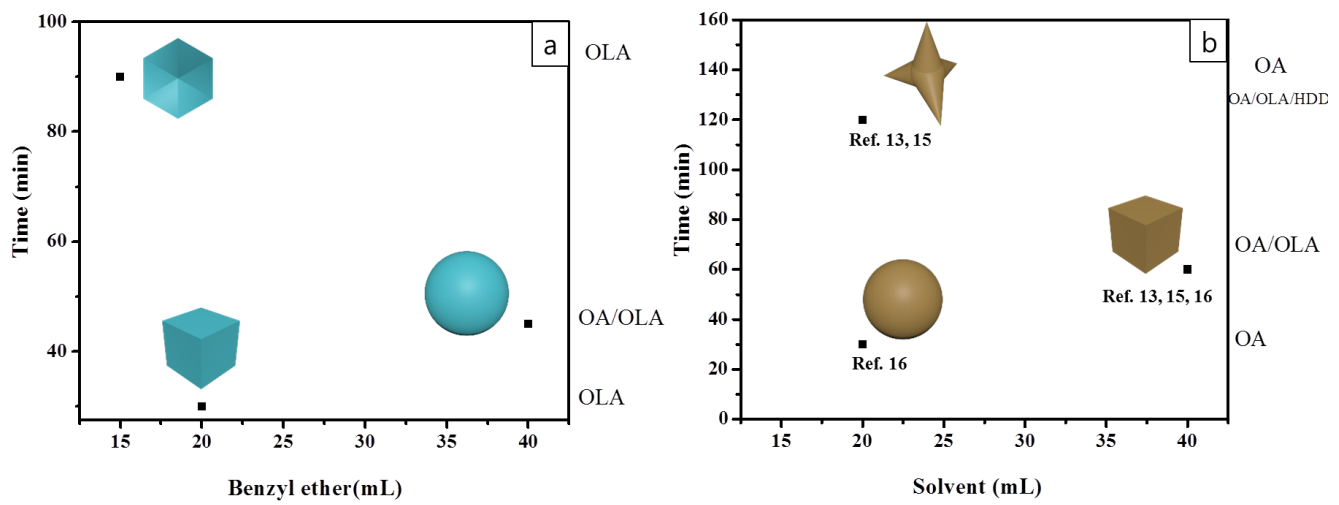


Figure 3-4. Schematic diagram of morphological evolution of  $\text{CoFe}_2\text{O}_4$  NPs under different synthetic conditions  
 (a) In case of this study and (b) In case of other reported works. [48,49,50]

produced a hexagonal shapes of  $\text{Fe}_3\text{O}_4$  NPs as appears clearly in Fig. 2 c, d and the average particles size increased to be 85.5 nm. The formation of the hexagonal shapes here may be attributed to the continuous growth at 290 °C along the corners of the cubic shape. For more detail of magnetite NPs structure, we used HRTEM to observe the single-crystallinity of the  $\text{Fe}_3\text{O}_4$  nanocubes as appear in Fig. 3. The interplanar distance measured from the adjacent lattice fringes in Fig. 3b is about 0.48 nm, which corresponding to (111) planes of the  $\text{Fe}_3\text{O}_4$  single crystal with cubic inverse spinel structure.[56,57] For easy understand of the relation between the reaction parameters and morphology controlling, Fig. 4 shows a schematic diagram for the morphological evolution of  $\text{CoFe}_2\text{O}_4$  NPs under different synthetic conditions. Fig. 4a represents the schematic of the obtained nanoparticles in our study within the three different shapes of sphere, cubes and hexagons. And, Fig. 4b concluded the other recently reported works for the synthesis of the various shapes of  $\text{CoFe}_2\text{O}_4$  NPs. Lu et al. and Zhang et al. reported the synthesis of two different shapes of cubes and star-like  $\text{CoFe}_2\text{O}_4$  NPs, however, Baaziz et al. synthesized two shapes of cubes and sphere  $\text{CoFe}_2\text{O}_4$  NPs using thermal decomposition method.[50]

Fig. 5 shows the EDS spectrum analysis for both samples of  $\text{CoFe}_2\text{O}_4$  and  $\text{Fe}_3\text{O}_4$  NPs. From the figure, there are mainly three elements of iron, oxygen and cobalt were observed for the  $\text{CoFe}_2\text{O}_4$  NPs sample (Fig. 5a), however, only iron and oxygen were detected for the second sample of  $\text{Fe}_3\text{O}_4$  NPs (Fig. 5b), confirmed the elemental composition of both samples. Since, because we employed the carbon copper grid in the measurements, there are two additional peaks in the spectrum for Cu and C were detected.

The crystal structure, phases and purity of the as-synthesized  $\text{CoFe}_2\text{O}_4$  and  $\text{Fe}_3\text{O}_4$  nanoparticles were investigated through the X-ray diffraction (XRD) with Cu K $\alpha$  radiation ( $\lambda = 1.540562\text{\AA}$ ). Fig. 6 shows the XRD diffraction patterns of the three different shapes of sphere,

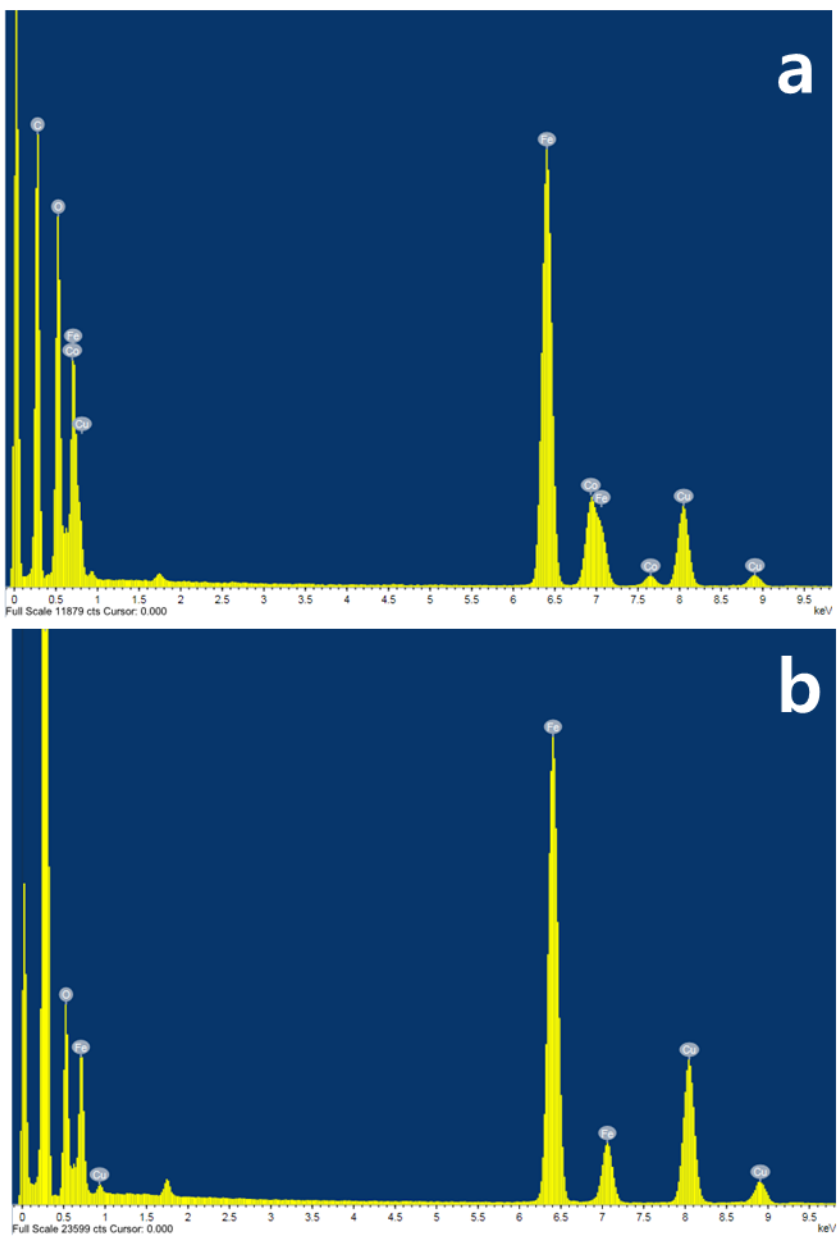


Figure 3-5. EDS elemental analysis of (a)  $\text{CoFe}_2\text{O}_4$  NPs and (b)  $\text{Fe}_3\text{O}_4$  NPs

cube and hexagonal CoFe<sub>2</sub>O<sub>4</sub> nanoparticles. From the figure, it is found that all of the diffraction peaks in the three patterns of the crystal planes (220), (311), (222), (400), (422), (511), and (533) could be indexed to a cubic inverse spinel structure of CoFe<sub>2</sub>O<sub>4</sub> NPs, which are consistent with the standard data for the ferrite phase (JCPDS card no.00-019-0629).[40] Additionally, no other impurity phases were detected in the patterns, reflecting the high purity phase of the as-synthesized CoFe<sub>2</sub>O<sub>4</sub> nanoparticles under current mild experimental condition. Further, the crystallite particle size of the three shapes of CoFe<sub>2</sub>O<sub>4</sub> nanoparticles were calculated from the XRD pattern using Debye-Scherrer formula of ( $D = K \lambda / \beta \cos \theta$ ), where  $\lambda$  is the X-ray wavelength (1.540562 Å),  $\beta$  is the full width at half maximum (FWHM),  $\theta$  is the Bragg angle for the studied peak/ring, and  $K$  is the shape factor which is normally taken as 0.9 for ferrites,[57,58] Based on the calculation, we found an agreement between the calculated crystallite particle size from XRD data (7.5 nm) and the estimated particles size from the TEM images(6.5 nm) for the sphere shape of CoFe<sub>2</sub>O<sub>4</sub> NPs, and it's may be attributed to the good dispersion of the sample as appeared from the TEM images. However, a disagreement between the calculated crystallite particle size from XRD data (19.5 and 23.5 nm) and the estimated particles size from the TEM images (66.6 and 98 nm) was found for the cubic and hexagonal shapes, respectively of CoFe<sub>2</sub>O<sub>4</sub> NPs, and this difference may be attributed to the polydispersity nature of the nanoparticles as displayed from the TEM images.

On the other hand, synthesized Fe<sub>3</sub>O<sub>4</sub> nanoparticles with two shapes of cubic and hexagonal displayed the same crystal planes and indexed to a cubic inverse spinel structure of Fe<sub>3</sub>O<sub>4</sub> within sharp and high intensity peaks (Fig 7). Further, even though it's too difficult to distinguish between the two phases of magnetite and maghemite through the XRD peaks, but the obtained completely black color in our samples, may be suggest that the magnetite is the dominant phase.[60] The lattice parameters were calculated using the following

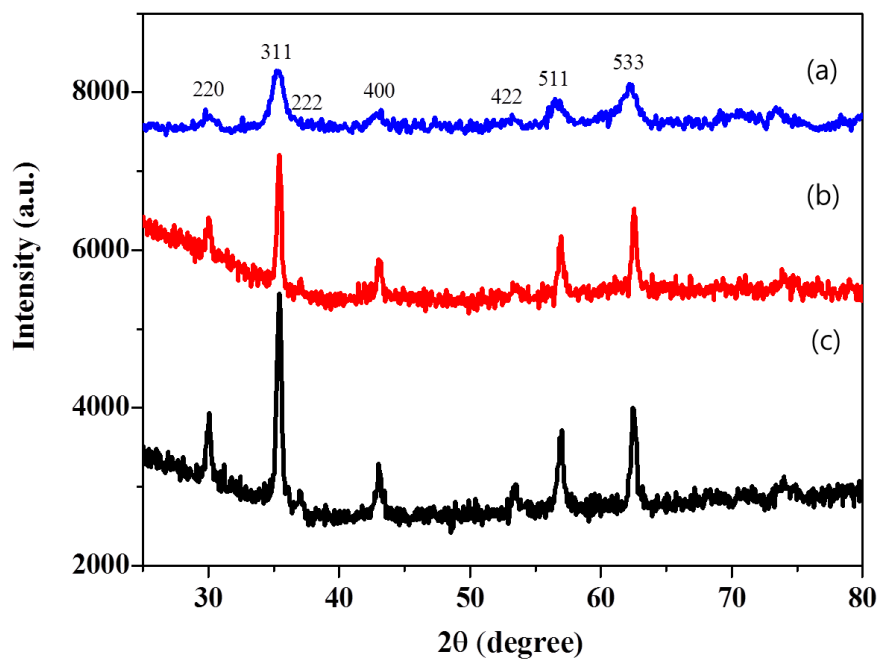


Figure 3-6. X-ray diffraction patterns of samples of (a)  $\text{CoFe}_2\text{O}_4$  nanosphere, (b)  $\text{CoFe}_2\text{O}_4$  nanocubes and (c)  $\text{CoFe}_2\text{O}_4$  nanohexagonal.

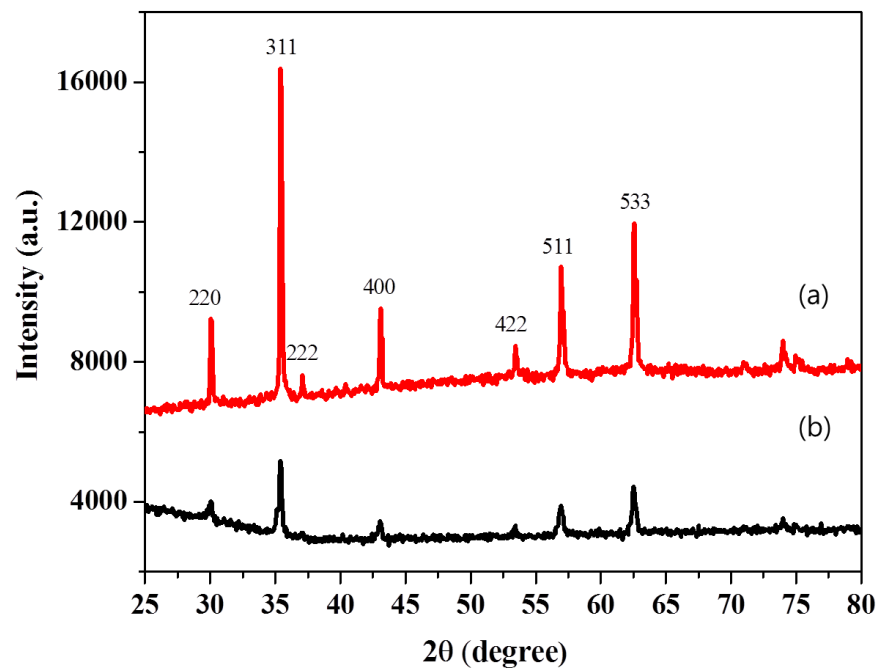


Figure 3-7. X-ray diffraction patterns of samples of (a)  $\text{Fe}_3\text{O}_4$  nanocubes, (b)  $\text{Fe}_3\text{O}_4$  nanohexagonal.

equations (1 and 2).[61,62] Using these equations, we calculated the lattice parameter of magnetite NPs to be (8.399 Å), which is more close to the standard lattice parameter of magnetite (8.396 Å).[63]

To calculate the lattice constant:

$$d = a_0 / \sqrt{h^2 + k^2 + l^2} \quad (3-1)$$

$$n\lambda = 2d \sin \theta \quad (3-2)$$

where d is line spacing between planes which can be calculated by Bragg's equation, and a is lattice constant; (hkl) is the indexing plane of atoms which can be obtained from X-ray diffraction data.[64]

The room temperature hysteresis loops of CoFe<sub>2</sub>O<sub>4</sub> and Fe<sub>3</sub>O<sub>4</sub> nanoparticles were measured by superconducting quantum interference device (SQUID) at applied field from -15 kOe to +15 kOe. The saturation magnetization value (M<sub>S</sub>) of CoFe<sub>2</sub>O<sub>4</sub> nanoparticles are 61.1, 80.9 and 76.4 emu/g for the three different shapes of sphere, cube, and hexagonal, respectively (Fig. 8). Hence, it's well known that, the particles with high degree of crystallinity have a surface with negligible spin canting and consequently high magnetic moment value.[65] In our samples, the obtained high magnetic moments values for both of cube and hexagonal CoFe<sub>2</sub>O<sub>4</sub> nanoparticles is attributed to their high crystallinity structure as clearly appeared and discussed above from the XRD data and TEM images, however, the relatively low magnetization value of 61.1 emu/g for the CoFe<sub>2</sub>O<sub>4</sub> NPs sample with sphere shape is may be due to its poor crystallinity and small particle size. The coercivity values (H<sub>c</sub>) of the three shapes of sphere, cube and hexagonal CoFe<sub>2</sub>O<sub>4</sub> nanoparticles are 439.4, 719.7 and 424.2 Oe, respectively. The difference in the coercivity values with particle size of CoFe<sub>2</sub>O<sub>4</sub> nanoparticles is may be related to the basis of domain structure, critical size, and the crystalline anisotropy.[67-70]

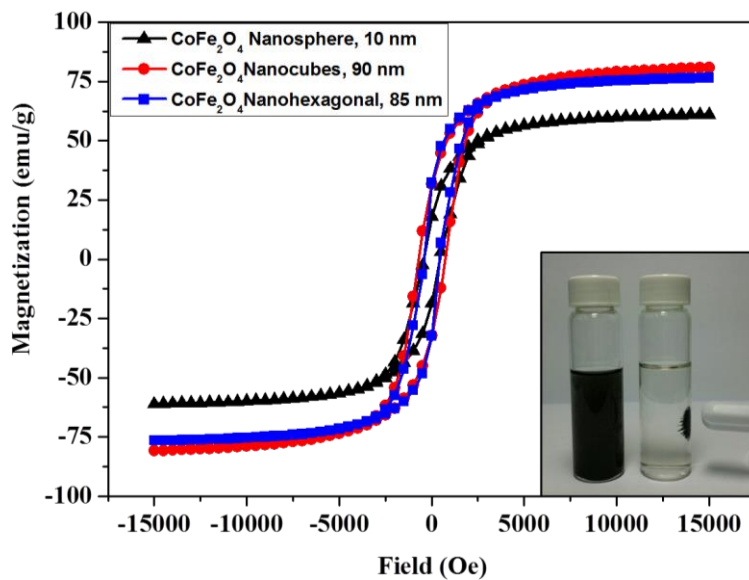


Figure 3-8. Hysteresis loops of  $\text{CoFe}_2\text{O}_4$  nanoparticles measured using SQUID at 300 K and a photograph of  $\text{CoFe}_2\text{O}_4$  NPs in solution in the absence and presence of an external magnet.

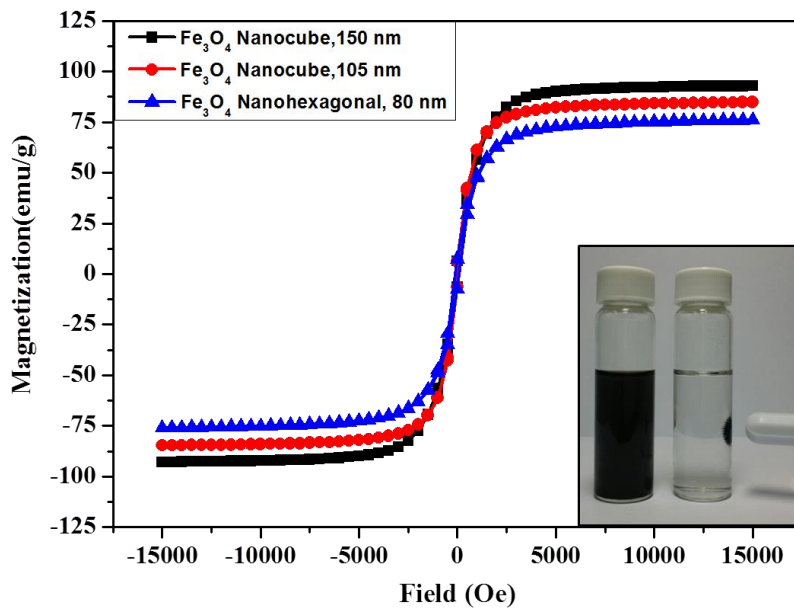


Figure 3-9. Hysteresis loops of  $\text{Fe}_3\text{O}_4$  nanoparticles measured using SQUID at 300 K and a photograph of  $\text{Fe}_3\text{O}_4$  NPs in solution in the absence and presence of an external magnet

Fig. 9 shows the magnetization curves for the Fe<sub>3</sub>O<sub>4</sub> nanocubes and nanohexagonal. The saturation magnetization value (M<sub>s</sub>) of Fe<sub>3</sub>O<sub>4</sub> are 92.9, 84.7 and 76 emu/g. The difference in the magnetization values in this case of Fe<sub>3</sub>O<sub>4</sub> nanoparticles is also may be due to the difference in the particles size. Apparently, M<sub>s</sub> decreases with decreasing particles sizes, and such decrease is ascribed to the surface spin canting and large surface to volume ratio of small nanoparticles.[71,72] The coercivity value (H<sub>C</sub>) of the three samples of Fe<sub>3</sub>O<sub>4</sub> are 90.9, 83.3 and 113.6 Oe, respectively. Because of their high magnetic moment values, both of CoFe<sub>2</sub>O<sub>4</sub> and Fe<sub>3</sub>O<sub>4</sub> nanoparticles can be rapidly separated from solution using an external magnetic field (inset of Fig. 8, 9).

### 3.4. Conclusions

In summary, a facile thermal decomposition approach was successfully designed for the synthesis of highly crystalline CoFe<sub>2</sub>O<sub>4</sub> and Fe<sub>3</sub>O<sub>4</sub> nanoparticles. Transmission electron microscopy results showed that, three shapes of sphere, cube and hexagonal nanoparticles were obtained through the easy modification of reaction parameters. The CoFe<sub>2</sub>O<sub>4</sub> and Fe<sub>3</sub>O<sub>4</sub> nanocubes showed the highest magnetic moment values among all of the other nanoparticle shapes. The simple thermal decomposition approach adopted in our work seems to be a very promising route for synthesis of various shapes and sizes of magnetic ferrite materials.

## **IV. The synthesis of FePt and FePt/Fe<sub>3</sub>O<sub>4</sub> nanoparticles**

### **4.1 Introduction**

Iron platinum (FePt) magnetic nanoparticles have been of great interest recently because of their chemical stability and potential various applications catalysis, energy and bio-applications [73]. Moreover, the biocompatibility properties of FePt nanoparticles enhanced its application in biomedicine fields, like target drug delivery, magnetic resonance imaging, hyperthermia, etc [74,79]. Therefore, many groups have put their efforts for synthesis of various shapes and sizes of FePt NPs using different synthesis approaches, like polyol, thermal decomposition, and chemical method, etc [76,77].

Hence, the thermal decomposition route has been considered as the best approach for synthesis of monodisperse and uniform magnetic nanoparticles. Thus, in my thesis, I succeeded to produce a 10 nm of cubic FePt NPs using a facile and convenient thermal decomposition method. Various parameters including ratio of precursor, reaction time, temperature were employed to control the morphology, atomic composition, magnetic properties and specific properties of FePt nanoparticles.

Because of its fascinating and very interesting optical, physical and thermal properties and the potential applications of the heterodimer materials, I succeeded using difference reducing agent, to not only synthesis of homogeneous FePt NPs but also heterodimer structure of FePt/Fe<sub>3</sub>O<sub>4</sub> NPs. High percent of Iron precursor ratio in the reaction vessel, resulted not to produce higher iron composition in FePt NPs, but they grow on surface of FePt nanoparticles and forming the heterodimer of FePt/Fe<sub>3</sub>O<sub>4</sub> NPs. So we could understand that energy of nucleation on particle surface is smaller than energy of separated Fe<sub>3</sub>O<sub>4</sub> nucleation [85].

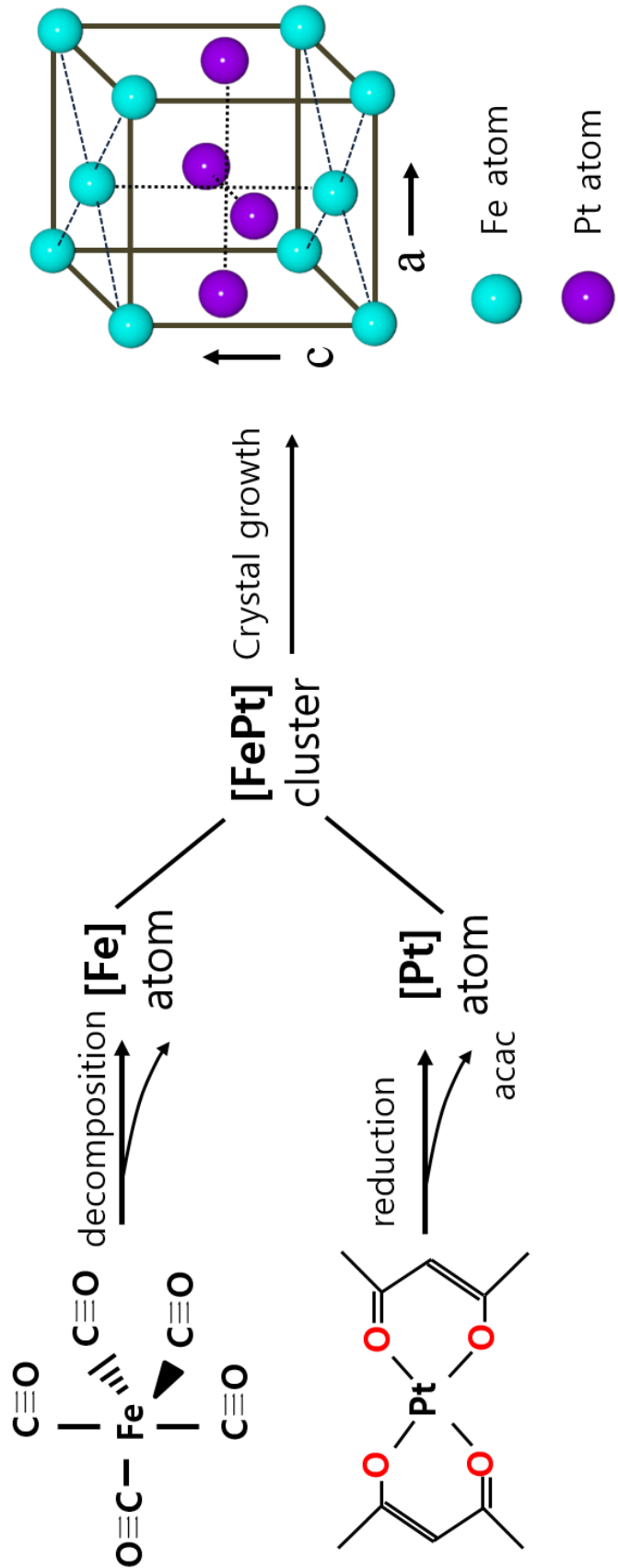


Figure 4-1. Schematic of FePt nanoparticles formation from decomposition of  $\text{Fe}(\text{CO})_5$  and reduction of  $\text{Pt}(\text{acac})_2$ .

## **4.2 Experiment section**

### **4.2.1 Materials**

Iron pentacarbonyl, platinum(II) acetylacetone (97%), octyl ether (99%), oleic acid (90%), oleylamine (70%), 1,2-hexadecanediol(90%) were purchased from Sigma-Aldrich, Ltd. 1-octadecene(95%) were purchased from Fluka. All of the chemicals were of analytical reagent grade and used as received without any further purification.

### **4.2.2 Synthesis of FePt nanoparticles**

Cubic FePt nanoparticles and FePt/Fe<sub>3</sub>O<sub>4</sub> NPs were synthesized in my thesis using facile thermal decomposition method through using different precursor molar ratio and reducing agent. Firstly, for synthesis of two kinds of nanoparticles (FePt and FePt/Fe<sub>3</sub>O<sub>4</sub>), suitable amount of platinum(II) acetylacetone, 4 mL octyl ether, 5 mL octadecene, 3 mL oleic acid and 3 mL oleylamine were dispersed in three neck round-bottom flask using mechanical stirrer. The mixture was heated to 120 °C with a heating rate of 5 °C min <sup>-1</sup>under Ar condition . Then, suitable amount of Iron pentacarbonyl was added to the above solution. After that, the reaction temperature was increased to 240 °C with same heating rate and kept refluxing for 60 min. After cooling down naturally, the precipitate washed several times using ethanol and hexane and kept in hexane with as suitable amount of oleic acid and oleylamine. For synthesis of only homogeneous FePt nanoparticles, I used the same reactioen condition and chemical amounts mentioned above with just changing the reducing agent of 5 mL octadecene to be 1 g 1,2-Hexadecandiol.

#### **4.2.3 Synthesis of FePt using 1,2-Hexadecanediol**

We synthesized with different precursor mol-ratio between Iron pentacarbonyl and platinum(II) acetylacetone from 1:1 to 4:1. Firstly, Suitable amount platinum(II) acetylacetone, 4 mL octyl ether, 1 g 1,2-Hexadecanediol, 3 mL oleic acid and 3 mL oleylamine were mixed in three neck round-bottom flask using mechanical stirrer. The mixture was heated to 120 °C with a heating rate of 5 °C min<sup>-1</sup> and suitable amount Iron pentacarbonyl was added to solution. Thereafter, the reaction temperature was increased to 240 °C with same heating rate and kept refluxing for 60 min. After cooling down, the precipitate was washed with ethanol and hexane for five times and kept in hexane with little amount of oleic acid and oleylamine.

#### **4.2.4 Cell culture and cell viability**

THP-1 cell is a human monocytic cell line derived from an acute monocytic leukemia patient. THP-1 cells were cultured in RPMI1640 medium containing 10% fetal bovine serum and penicillin-streptomycin solution. Cells were grown and maintained in 100mm cell culture dish in humidified incubator at 37°C with 5% CO<sub>2</sub> and 95% air. Nanoparticles were sterilized by UV light treatment for 2-3 hours. Nanoparticle suspension was dispersed using sonication to prevent aggregation. Cells were treated with different concentration (62.5, 250, 1000 and 4000 µg/mL) of nanoparticles for specific times.

Cell viability was evaluated using a CCK-8 assay. The cell density of 3x10<sup>4</sup>/ml cells/well were seeded in 96-well tissue culture plates and allowed to grow for 8 hours in wells before nanoparticle treatment. Cells were treated with different concentration of nanoparticles for specific time. Wells without nanoparticles served as control. At the end of nanoparticle exposure after specific times, WST-8(CCK-8 kit) solution was added to each well and

incubated for 3-4 hours at 37°C as per manufacturer's instructions. At the end, absorbance was measured at 450 nm for each well using microplate spectrophotometer (Thermo Fisher). The viability of the treated samples was expressed as a percentage of non-treated control cell samples, assumed to be 100%. Morphological analysis was investigated using light microscope at 40X magnification and pictures were captured for using computerized digital camera.

Cell death was further confirmed from confocal images. Briefly, THP-1 cells were seeded in 24-well tissue culture plates and allowed overnight to grow in the wells; the cells were treated with nanoparticles for specific time. In order to distinguish live cells from dead cells, cultures were treated with the LIVE/DEAD® Cell-Mediated Cytotoxicity Kit (L7010) contents. In brief, after incubation, the culture medium was removed from each well and replaced with DiOC18. The amount of the DiOC18 staining solution required depends on the number of cells to be labeled. The cells were incubated in staining solution overnight under normal culture conditions. Next day, the cells were concentrated by centrifugation for about 5 min and washed with phosphate-buffered saline solution (pH 7.4) to remove excess staining. Cell pellets were resuspended in a counter staining solution (propidium iodide, PI) and incubated for 5 min at room temperature. After incubation the cells in PI, the cell mixture (10-20 µL) was taken and placed on a glass slide covered with a coverslip. Finally, the cells were visualized immediately under microscope. The images were acquired on an Inverted Axiovert confocal laser scanning microscope (CLSM) equipped with laser (VIS) and a scanning (META) module in an epifluorescence mode. The 488-nm line of an argon ion laser and the 543-nm line of a helium–neon laser were used to excite the samples. A DD 488/543 filter was used to separate the red/green fluorescence signals. Images were collected and saved using the software LSM (Zeiss image confocal software) and exported to save as TIFF or JPEG format. Cell viability was quantified by calculating the percentage of fluorescing cells.

#### **4.2.5 Characterization**

The morphology and size of the nanoparticles were measured using transmission electron microscopy (TEM, Tecnai G2 F20 TWIN TMP) and field emission transmission electron microscopy (FE-TEM, the Histachi HF-3300 at 300 kV) and nanoparticles composition ratio were analyzed by EDS which coupled with the TEM equipment. The crystal structures of the nanoparticles were analyzed using X-ray diffraction (XRD, Rigaku D/max-250) with Cu K $\alpha$  radiation ( $\lambda = 1.540562 \text{ \AA}$ ) in the  $2\Theta$  range from  $20^\circ$  to  $90^\circ$ . The magnetic properties were analyzed with vibrating sample magnetometer (VSM, Lakeshore 7407) from -10 kOe to +10 kOe at room temperature.

### **4.3 Results and Discussion**

A facile, reliable and effective thermal decomposition route was designed in my thesis for synthesis of two kinds of FePt NPs of cubic shape and heterodimer structure of FePt/Fe<sub>3</sub>O<sub>4</sub> nanoparticles. Although it's difficult to synthesis of homogeneous FePt nanoparticles through the thermal decomposition method because of their decomposition rate, in this thesis, I succeeded to optimize the suitable reaction condition for synthesis of both cubic FePt nanoparticles and also heterodimers of FePt/Fe<sub>3</sub>O<sub>4</sub> nanoparticles using two different reducing agent of 1-octadecene and 1,2-hexadecandiol and also through changing the molar ratio of the precursor.

When I used 1-octadecene as reducing agent, a heterodimer structure shape of FePt/Fe<sub>3</sub>O<sub>4</sub> was resulted instead of the expected FePt nanoparticle alloy. The reason is may be understood in terms of the energy of nucleation on particle surface is smaller than energy of separated Fe<sub>3</sub>O<sub>4</sub> nucleation [83-85]. Also, the nonpolar solvent which I used in my experiment influenced on heteroepitaxial nucleation [86].

Figure 4-3. shows TEM images of cubic FePt synthesized with precursor ratio from 1:1 to 4:1 using 1-octadecene. Cubic FePt of  $5 \sim 10$  nm size was obtained using our experiment condition. And In figure 4-2, the composition ratio at point ①, ②, ③, ④ gives the nanostructure as shown in the figure 4-3. ①, ②, ③, ④ respectively. The variation of FePt nanoparticles atomic composition were measured by EDX. With 1-octadecene, iron composition ratio increase with more iron precursor. However, over the 4:1 precursor ratio, hetero-dimer structure was formed and the dark part is FePt nanoparticles and the light part is  $\text{Fe}_3\text{O}_4$  nanoparticles. On the other hand, when I used 1,2-hexadecandiol as reducing agent, iron composition ratio of FePt nanoparticles increase with more iron precursor. However, unlike synthesized nanoparticles with 1-octadecene, even over the 4:1 precursor ratio, they did not show heterodimer structures. And FePt atomic composition ratio could be controlled easily with 1,2-hexadecandiol.

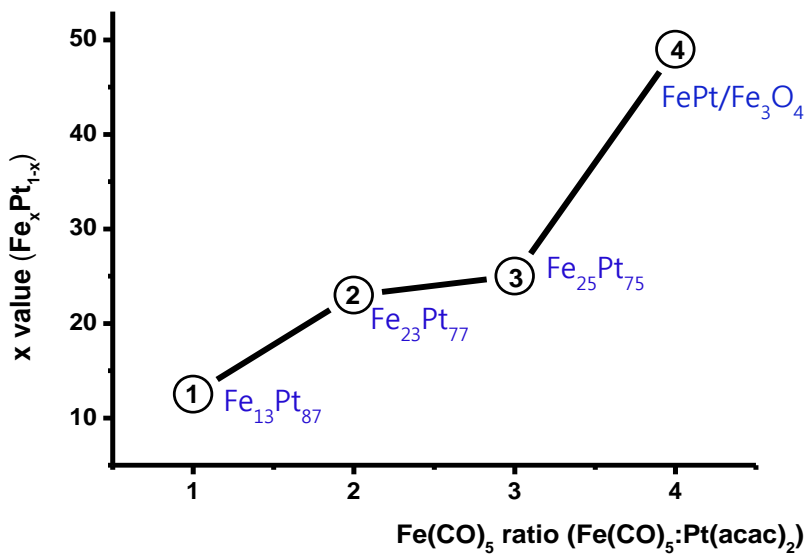


Figure 4-2. Variation in iron composition ratio of FePt nanoparticles with different precursor ratio.

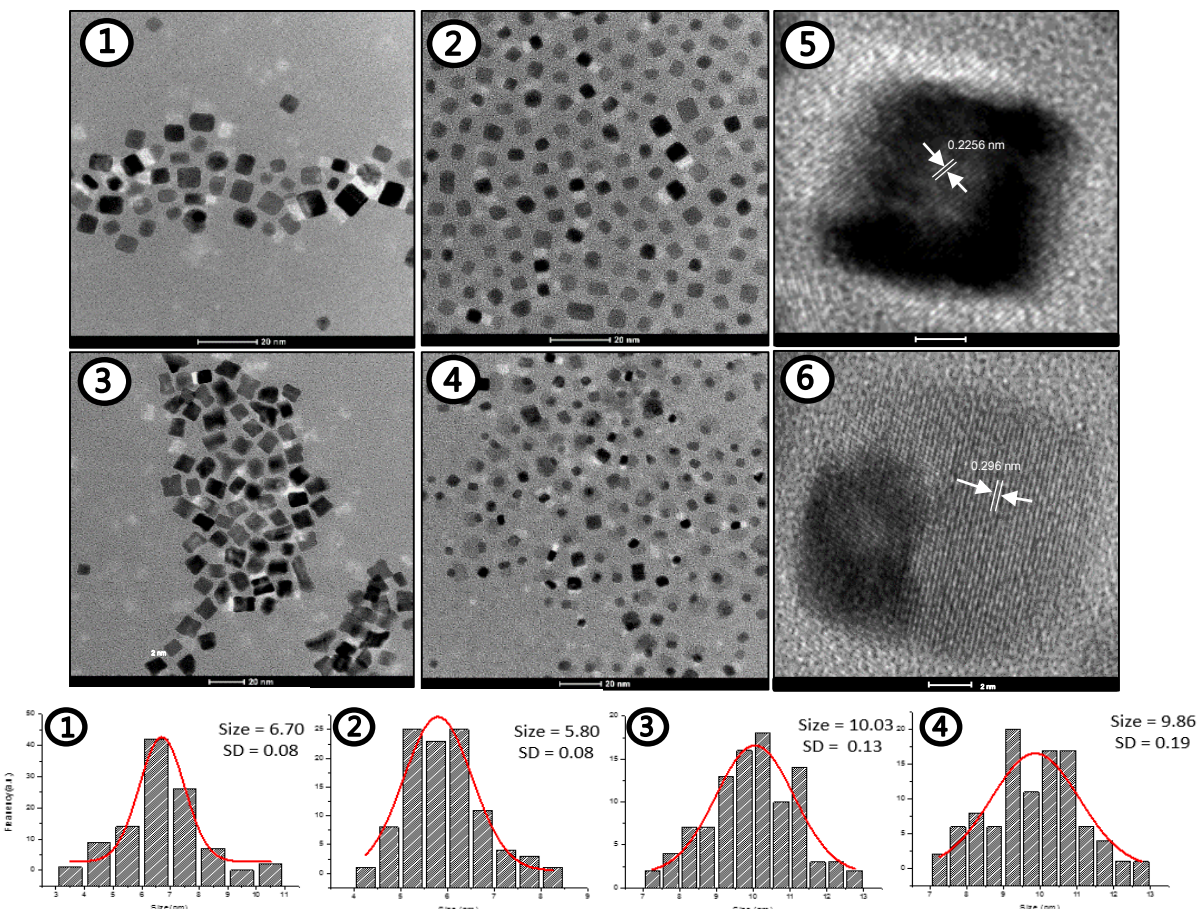


Figure 4-3. TEM images and Size distribution of FePt nanoparticles with different precursor ratio.

①  $\text{Fe}(\text{CO})_5 : \text{Pt}(\text{acac})_3 = 1 : 1$ , ②  $2 : 1$ , ③  $3 : 1$ , ④  $4 : 1$

⑤ HRTEM of a single FePt nanocube, ⑥HRTEM of  $\text{FePt}/\text{Fe}_3\text{O}_4$  heterostructure.

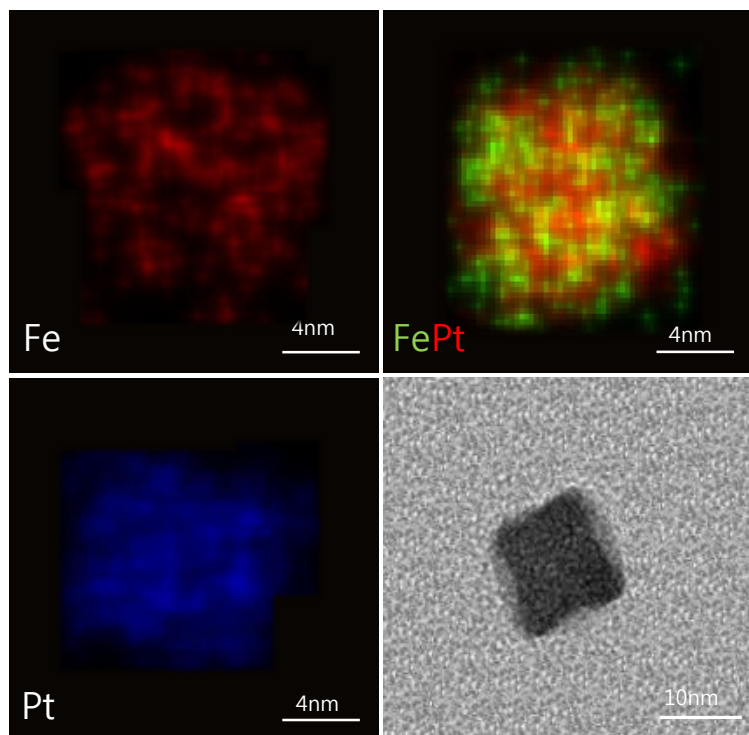


Figure 4-4. The EDS mapping images of synthesized homogeneous FePt nanoparticle using 1-octadecene.

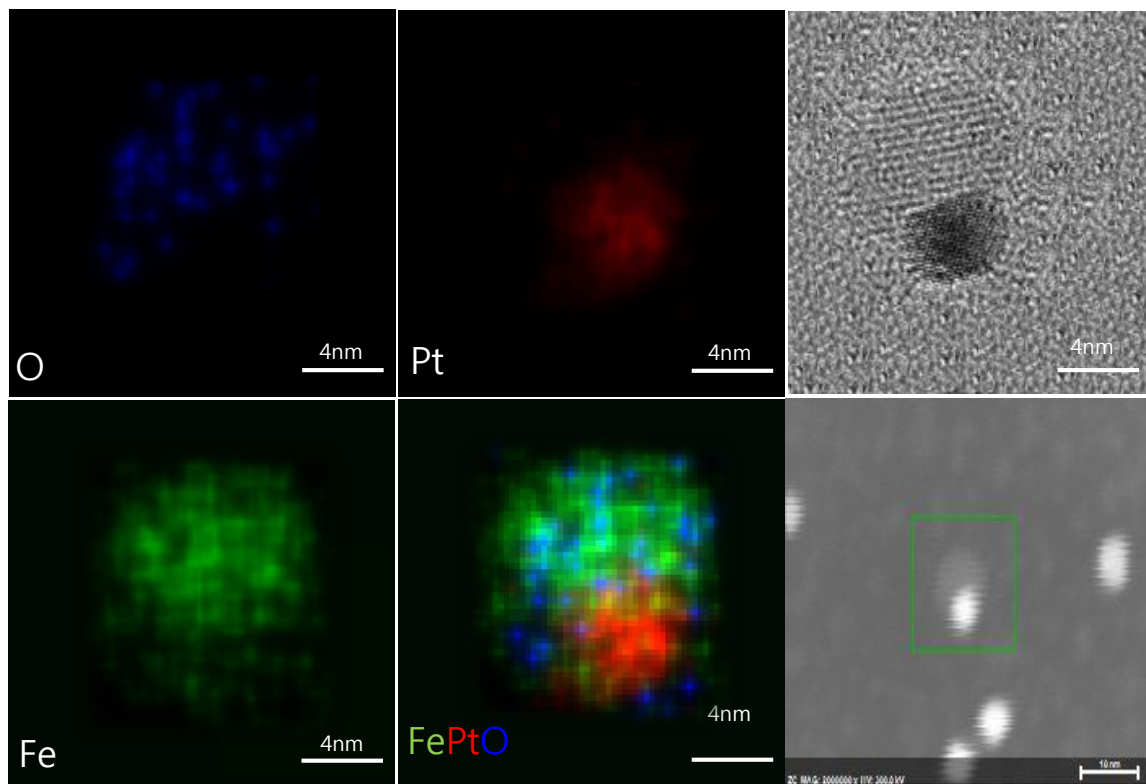


Figure 4-5. The EDS mapping images of synthesized heterodimer structure FePt/Fe<sub>3</sub>O<sub>4</sub> using 1-octadecene.

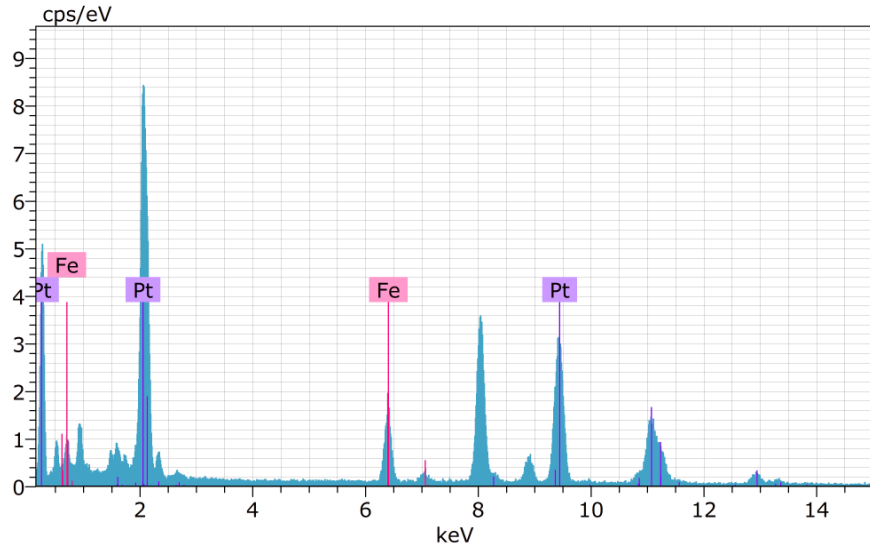


Figure 4-6. The EDS elemental analysis of FePt nanoparticles.

Figure 4-3. ⑤, ⑥ were characterized with HRTEM and show clearly the lattice fringes of the nanoparticles. Figure 4-3. ⑤ show lattice fringes of {111} plane for FePt and its distance between planes (0.225 nm) is close to calculated value with XRD pattern (0.22561 nm). And Figure 4-3. ⑥ show lattice fringes of {220} plane for  $\text{Fe}_3\text{O}_4$  and its distance between planes (0.296 nm) is close to calculated value with XRD pattern (0.29624 nm). Measuring size and standard deviation of FePt nanoparticles was carried out with counting 100 particles using lognormal distribution.

Figure 4-4., 4-5. show the EDX mapping images of FePt and  $\text{FePt}/\text{Fe}_3\text{O}_4$  using 1-octadecene with different precursor ratio. First, synthesized FePt nanoparticles have randomly ordered structure. Actually, without annealing process, chemically disordered FePt was synthesized and completely ordered  $\text{L1}_0$  FePt could be obtained with annealing process at minimum 550 °C for 30 min. And figure 4-5. Also support hetero structure consist of FePt and  $\text{Fe}_3\text{O}_4$ .

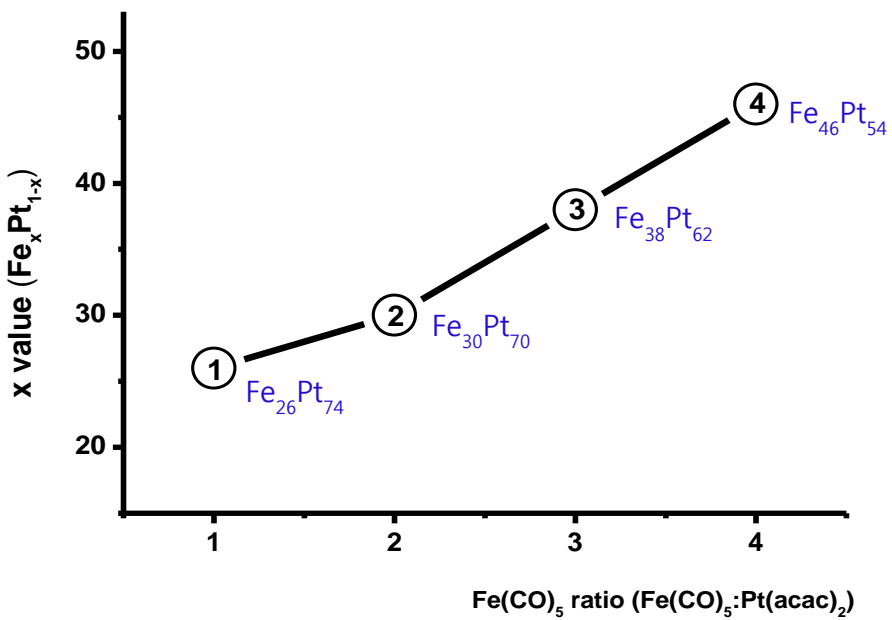


Figure 4-7. Variation in iron composition ratio of FePt nanoparticles with different precursor ratio.

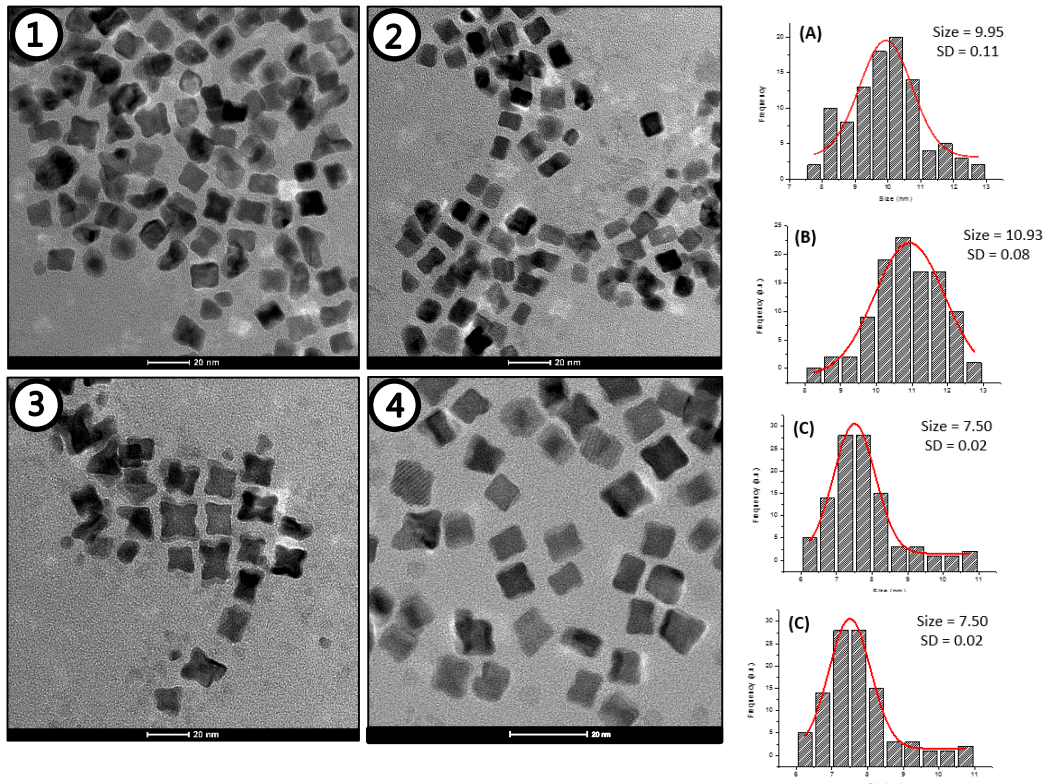


Figure 4-8. TEM images and Size distribution of FePt nanoparticles with different precursor ratio.

Fe(CO)<sub>5</sub> : Pt(acac)<sub>3</sub> = 1 : 1, ② 2 : 1, ③ 3: 1, ④ 4: 1.

The synthesized FePt using 1-octadecene has increasing Ms value with increasing Fe precursor: Ms= 0.07 emu/g at ratio 1:1, Ms= 3.67 emu/g at ratio 2:1, Ms= 12.93 emu/g at ratio 3:1. And FePt/Fe<sub>3</sub>O<sub>4</sub> hetero structure have the highest Ms value due to formation Fe<sub>3</sub>O<sub>4</sub> phase. And the synthesized FePt using 1,2-hexadecandiol has increasing Ms value with increasing Ms value like synthesized FePt using 1-octadecene. Synthesized FePt nanoparticles have no coercive value and show superparamagnetic properties.

The crystal structure of the nanoparticles was analyzed using X-ray diffraction (XRD, Rigaku D/max-250) with Cu K $\alpha$  radiation ( $\lambda = 1.540562 \text{ \AA}$ ) in the  $2\Theta$  range from  $20^\circ$  to  $90^\circ$ . Figure 4-10 shows XRD diffraction patterns of the synthesized FePt nanoparticles and FePt/Fe<sub>3</sub>O<sub>4</sub> NPs when used 1-octadecene as reducing agent . In figure 4-10, there are 4 kinds of diffraction pattern with different precursor ratio from 1:1 to 4:1 using 1- octadecene. Crystal planes of (111), (200), (220) of FePt were found and well matched with the standard data for fcc FePt (JCPDS card no. 00-029-0718). With increasing the precursor ratio, crystal planes of (220), (311), (400), (511), (533) of Fe<sub>3</sub>O<sub>4</sub> were found and also well matched with the standard data for spinel Fe<sub>3</sub>O<sub>4</sub> (JCPDS card no. 00-019-0629). However, when I used 1,2-hexadecandiol as reducing agent , the diffraction pattern of Fe<sub>3</sub>O<sub>4</sub> peak couldn't detect and only the peaks which consistent with the standard data for fcc FePt (JCPDS card no. 00-029-0718) is detected, which confirming the formation of pure phase of FePt nanoparticles [78].

Figure 4-11. shows the cytotoxicity evaluated by 96 well assay in range of 62.5, 250, 1000, 4000  $\mu\text{g/ml}$  of FePt nanoparticles for 24 hours and 48 hours. Higher concentration of FePt showed inhibitory effect on cell growth. Especially, THP-1 cell viability decrease 40 % at 4000  $\mu\text{g/ml}$  of FePt nanoparticles. So for bio-application of FePt nanoparticles with more high concentration, studies for increasing biocompatibility are needed. And there are many ligand change to increase cell viability with PEG, cysteamine, silica and so on.[79-81]

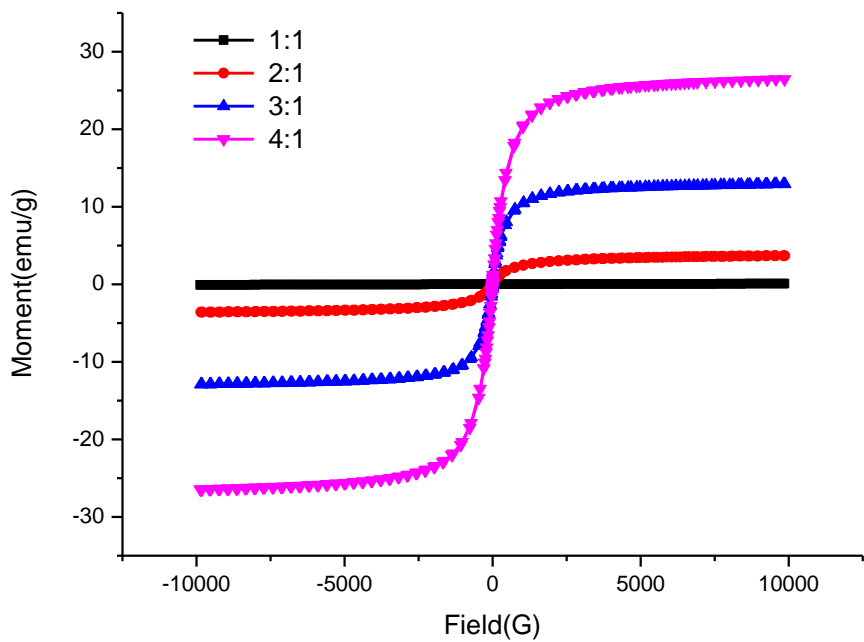


Figure 4-9. The hysteresis loops of FePt nanoparticles with different precursor ratio at 300 K.

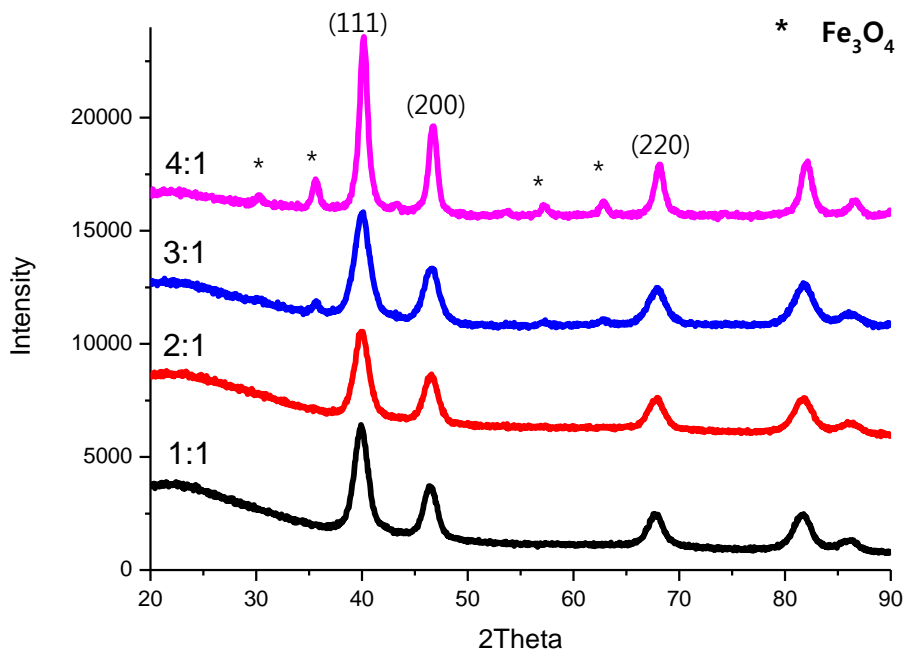
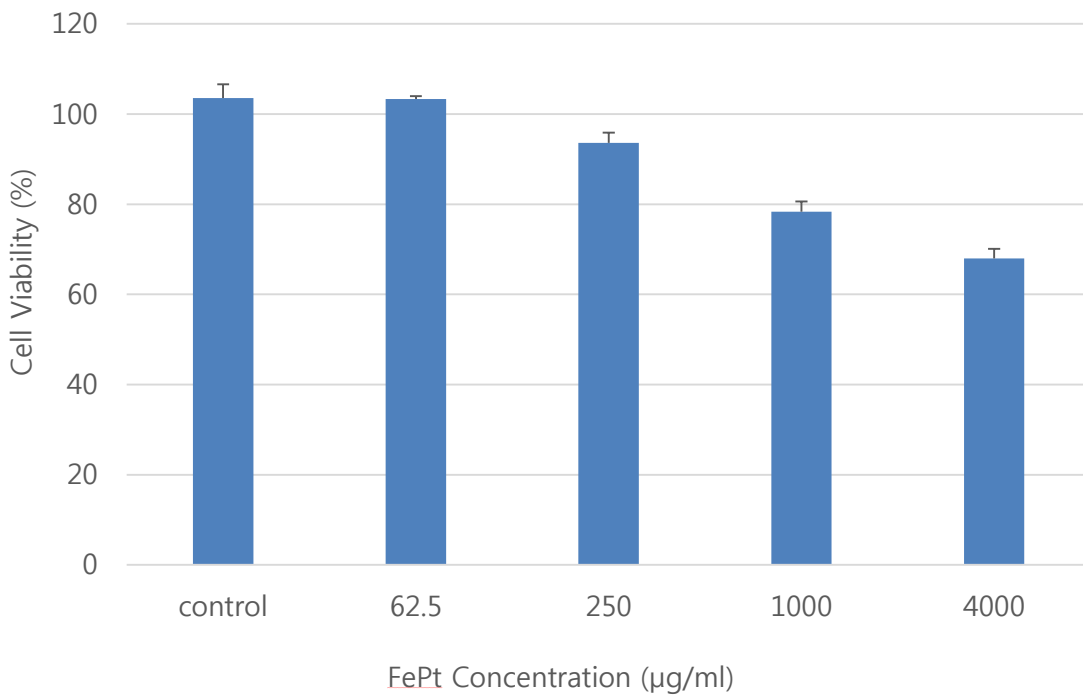


Figure 4-10. The XRD patterns of FePt nanoparticles with different precursor ratio.

Figure 4-12. shows the image of stained live and dead cell and easily check and quantify for cell viability in each concentration. For staining, DIOC18 and propidium iodide were used. 3,3'-dioctadecyloxacarbocyanine perchlorate (DIOC18) can react with cell membrane by two C18 alkyl chains and stain cell membrane with a green fluorescent dye. And propidium iodide can penetrate only dead cell and stain their nuclei with red fluorescent dye. Live cells show only stained green cell membrane image and dead cells show both stained green cell membrane and red nuclei image [82]. And with low concentration, THP-1 cell almost live. But with high concentration, some stained red cell were found. So we checked cell viability visually depending on difference concentration which have an effect for cell live condition.

**In this thesis**, I synthesized FePt nanoparticles through using two kinds of reducing agent (1-octadecene, 1,2-hexadecandiol). Each reducing agent shows different result. One is FePt cubic nanoparticles and the other is FePt/Fe<sub>3</sub>O<sub>4</sub> NPs. Because they have different electron donating group that means they have difference of redox potential. Hydroxide functional group have more activating power for electron donating. So synthesis of FePt nanoparticles using 1,2-hexadecandiol didn't show hetero-dimer structure. With this result, we could get an important parameter for controlling morphology of nanoparticles.

(a) 24 Hours



(b) 48 Hours

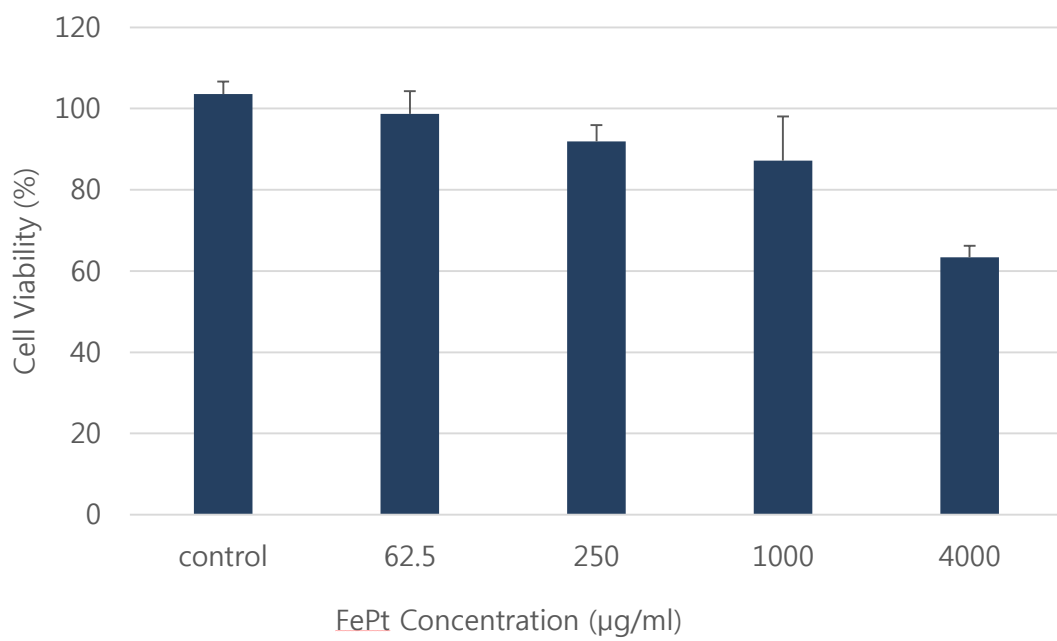


Figure 4-11. The Cytotoxicity evaluated by 96 well assay in rage of 62.5 – 400  $\mu\text{g}/\text{ml}$  of FePt nanoparticles

(A) 24 Hours, (B) 48 Hours.

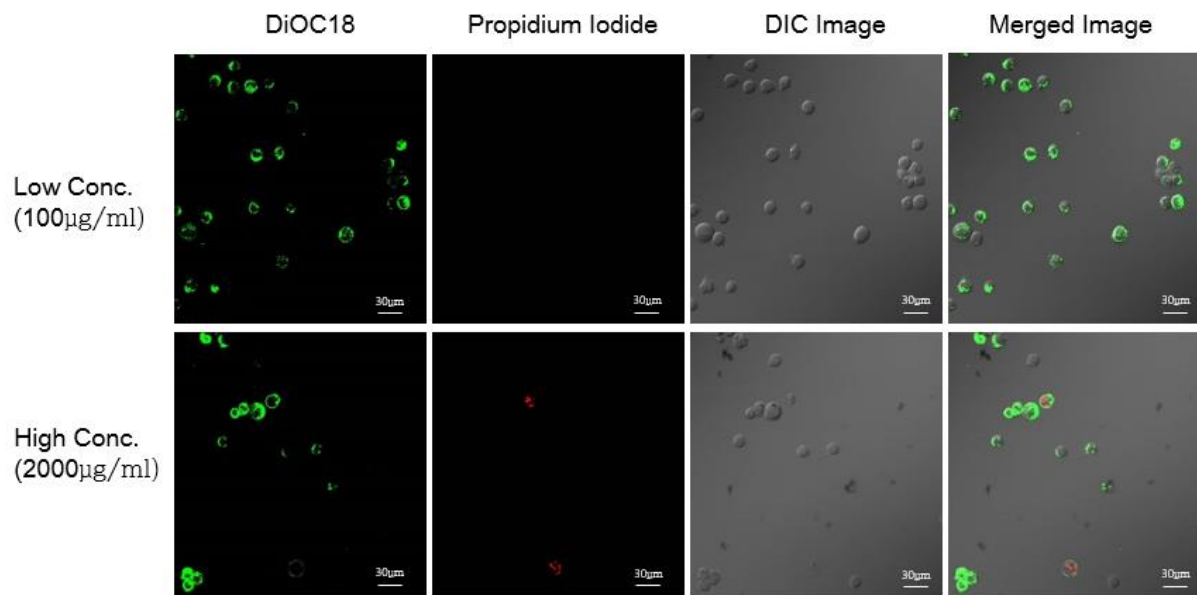


Figure 4-12. THP-1 Cells treated different concentration of FePt for 24 hours and stained with LIVE/DEAD staining solution.

#### 4.4 Conclusion

In summary, I succeeded to synthesis of FePt nanoparticles with two morphology shapes of cubic FePt and heterodimer structure of FePt/Fe<sub>3</sub>O<sub>4</sub> NPs using simple and effective thermal decomposition method. XRD and TEM results were used to confirm the both structure and shape of homogenous cubic FePt and FePt/Fe<sub>3</sub>O<sub>4</sub> nanoparticles. The facile thermal decomposition route adopted in my thesis seems to be a very promising and effective for synthesis of various shapes and sizes of FePt nanoparticles.

## References

- [1] X. Batlle, A. Labarta, Finite-size effects in fine particles: magnetic and transport properties, *J. Phys. D: Appl. Phys.*, 35, 2002, R15.
- [2] P. Buffat, J. P. Borel, Size effect on the melting temperature of gold particles, *Phys. Rev. A* 13, 1976, pp. 2287-2298.
- [3] C. N. R. Rao, A. Müller, A. K. Cheetham, *The Chemistry of Nanomaterials: Synthesis, Properties and Applications*, Wiley-VCH, 2004, Chapter 1.
- [4] Z. L. Wang, *Characterization of Nanophase Materials*, Wiley-VCH, 2000.
- [5] S. C. Tjong, *Nanocrystalline Materials: Their Synthesis-Structure-Property Relationships and Applications*, Elsevier, 2006.
- [6] C.T Black, C.B Murray, R.L Sandstrom, S. Sun. *Science* 290, 2000, pp. 1131-1134.
- [7] G. Bate, in: Wohlfarth E-P., I980, *Ferromagnetic Materials*, Vol. 2.North- Holland; Amsterdam.
- [8] H. Zeng, J. Li, J.P. Liu, Z.L. Wang, S. Sun. *Nature*, 420, 2002, pp. 395-398.
- [9] Z.L. Lu, W.Q. Zou, L.Y Lv, X.C. Liu, S.D. Li, J.M. Zhu, F.M. Zhang, Y.W. Du, *J Phys Chem B*, 110, 2006, pp. 23817-23820.
- [10] Z.M. Liao, Y.D. Li, J. Xu, J.M. Zhang, K. Xia, D.P. Yu, *Nano. Lett.*, 6, 2006, pp. 1087-1091.
- [11] D. Zhang, Z. Liu, S. Han, C. Li, B. Lei, M.P. Stewart, J.M. Tour, C. Zhou, *Nano. Lett.*, 4, 2004, pp. 2151 – 2155.
- [12] X. Piao, G.M. Zeng , D.L. Huang, C.L. Feng , S. Hu, M.H. Zhao ,C. Lai, Z. Wei, C. Huang, G.X. Xie, Z.F. Liu, *Science of the Total Environment*, 424, 2012, pp. 1–10.
- [13] J.M. Jeong , B.G. Choi , S.C. Lee , K.G. Lee , S.J. Chang ,Y.K. Han , Y.B. Lee , H.U. Lee , S. Kwon , G. Lee ,C.L. Lee , Y.S. Huh, *Adv. Mater.* 25, 2013, pp. 6250–6255.
- [14] A.K. Gupta, M. Gupta, *Biomaterials*, 26, 2005, pp. 3995–4021.
- [15] J. Xie, J. Huang, X. Li, S. Sun and X. Chen, *Current Medicinal Chemistry*, 16, 2009, pp. 1278-1294.
- [16] Kinge, S., Calama, M. C., and Reinhoudt, D. N., Self-assembling nanoparticles at surfaces and interfaces, *Chem. Phys. Chem.*, 9, 2008, pp. 20–42.
- [17] Na, H. B., Song, I. C., and Hyeon, T. (2009). Inorganic nanoparticles for MRI contrast agents, *Adv. Mater.*, 21, pp. 2133–2148.

- [18] Klabunde, K. J. *Nanoscale Materials in Chemistry* (John Wiley & Son, Inc.), 2001.
- [19] Schmid, G. *Nanoparticles: From Theory to Application* (Wiley-VCH Verlag GmbH & Co. KgaA, Weinheim), 2004.
- [20] L. T. Lu, N. T. Dung, L. D. Tung, C. T. Thanh, O. K. Quy,N. V. Chuc, S. Maenosonoe and N. T. K. Thanh, *Nanoscale*, 7, 2015, pp. 19596.
- [21] R. Hufschmid, H. Arami, R. M. Ferguson, M. Gonzales, E. Teeman, L. N. Brush, N. D. Browning and K. M. Krishnan, *Nanoscale*, 7, 2015, pp. 11142.
- [22] K. Zhang, W. Zuo, Z. Wang, J. Liu, T. Li, B. Wang and Z. Yang, *RSC Adv.*, 5, 2015, pp. 10632.
- [23] W. Baaziz, B. P. Pichon, Y. Liu, J. M. Gren`eche, C. U. Bouillet, E. Terrier, N. Bergeard, V. Halt`e, C. Boeglin, F. Choueikani, M. Toumi, T. Mhiri and S. B. Colin, *Chem. Mater.*, 26, 2014, pp. 5063–5073.
- [24] Mahmood Aliofkhazraei, "Modern Surface Engineering Treatments", InTech, 2013.
- [25] B. D. Cullity, "Introduction to magnetic materials", Addison-Wesley Publishing Company, 1972, pp. 93.
- [26] Mohamed abbas, "Sonochemical synthesis of functionalized core/shell iron oxide nanocubes for catalytic and bio-applications", Ph.D. thesis, DGIST, Daegu, Republic of Korea, 2015, 172 pages.
- [27] SangIm Park, "Synthesis of magnetite core-lecithin shell colloid and its application in cancer therapy", Ph.D. thesis, Chungnam National University, Daejeon, Repubilc of Korea, 2007, 168 pages.
- [28] YoungWook Jun, JungWook Seo, JinWoo Cheon, "Nanoscaling Laws of Magnetic Nanoparticles and Their Applicabilities in Biomedical Sciences", *J. Accounts of chem. Research*, 2, 2008, pp. 179-189.
- [29] Ji Sung Lee, Jin Myung Cha, Ha Young Yoon, Jin-Kyu Lee, Young Keun Kim, "Magnetic multi-granule nanoclusters: A model system that exhibits universal size effect of magnetic coercivity", *Scientific reports*, 5, 2015.
- [30] D Dozier, S Palchoudhury, Y Bao, "Synthesis of iron oxide nanoparticles with biological coatings", *J. Science and Health at The University*, 2010.
- [31] Wei Wu, Quanguo He, Changzhong Jiang, "Magnetic Iron Oxide Nanoparticles: Synthesis and Surface Functionalization Strategies", *Nanoscale Research Letters*, 3, 2008, pp. 397.
- [32] Hosokawa Masuo, "nanoparticle technology handbook", Elsevier, 2012.
- [33] Peter W. Dunne, Alexis S. Munn, Chris L. Starkey, Tom A. Huddle, Ed H. Lester, "Continuous-flow hydrothermal synthesis for the production of inorganic nanomaterials", *philosophical transactions of the royal society A*, 2015, pp. 373.
- [34] B. D. Cullity, "Elements of X-ray Diffraction", Addison-Wesley, Publication Company Inc, Reading UK,

1956.

- [35] 고재귀, “자성재료학”, 송실대학교출판부, 2008.
- [36] D. Ling, T. Hyeon, Small , 2013, 9, 1450–1466.
- [37] J.M. Jeong , B.G. Choi, S.C. Lee , K.G. Lee , S.J. Chang ,Y.K. Han , Y.B. Lee , H.U. Lee , S. Kwon, G. Lee , C.S. Lee, Y. S. Huh, Adv. Mater 2013, 25, 6250–6255.
- [38] M.B. Gawande, P.S. Branco, R.S. Varma, Chem. Soc. Rev., 2013, 42, 3371-3393.
- [39] S.C. Goh, C.H.Chia, S. Zakaria, M.Yusoff, C.Y. Haw, S.H. Ahmadi, N.M. Huang, H.N. Lim, Materials Chemistry and Physics, 2010, 120, 31–35.
- [40] M. Abbas, B.P. Rao, M.N. Islam, K.W. Kim, S.M. Naga, M. Takahashi, C. Kim, Ceramics International, 2014, 40, 3269–3276.
- [41] F.N. Sayed, V. Polshettiwar, Scientific Reports, 5, 2015, 09733.
- [42] M. Abbas, B.P. Rao, C. Kim, Materials Chemistry and Physics, 2014, 147, 443-451.
- [43] Y.V. Kolen'ko, M.B. López, C.R. Abreu, E.C. Argibay, A. Sailsman, Y.P. Redondo, M.F. Cerqueira, D.Y. Petrovykh, K.I Kovnir, O.I. Lebedev, J. Rivas, J. Phys. Chem. C , 2014, 118 8691–8701.
- [44] Y. Lee, J. Lee, C.J. Bae, J.G. Park, H.J. Noh, J.H. Park, T. Hyeon, Advanced Functional Materials, 15, 2005, 3.
- [45] J. Park, K. An, Y. Hwang, J.G. Park, H.J. Noh, J.Y. Kim, J.H. Park, N.M Hwang, T. Hyeon, Nature Materials, 2004, 3.
- [46] T. Ahn, J.H. Kim, H.M. Yang, J.W. Lee, J.D. Kim, J. Phys. Chem. C, 2012, 116, 6069–6076.
- [47] M. Abbas, M. Takahashi, C. Kim, J Nanopart Res , 2013, 15,1354.
- [48] L.T. Lu, N.T. Dung, L.D. Tung, C.T. Thanh, O.K. Quy, N.V. Chuc, S. Maenosonoe, N.T.K. Thanh, Nanoscale, 2015, 7, 19596.
- [49] R. Hufschmid, H. Arami, R.M. Ferguson, M. Gonzales, E. Teeman, L.N. Brush, N.D. Browning, K.M. Krishnan, Nanoscale, 2015, 7, 11142.
- [50] G. Gao, X. Liu, R. Shi, K. Zhou, Y. Shi, R. Ma, E.T. Muromachi, G. Qiu, Journal of American Chemical Society, 2010, 10, 2888-2894.
- [51] D. Kim, N. Lee, M. Park, B.H. Kim, K. Jin, T. Hyeon, Journal of American Chemical Society, 2009, 131,454-455.
- [52] H. Yang, T. Ogawa, D. Hasegawa, M. Takahashi, Journal of Applied Physics, 103, 07D526.

- [53] K. Zhang, W. Zuo, Z. Wang, J. Liu, T. Li, B. Wang, Z. Yang, RSC Adv, 2015, 5, 10632.
- [54] 19 C. Hui, C. Shen, J. Tian, L. Bao, H. Ding, C. Li, Y. Tian, X. Shi, H.J. Gao, Nanoscale, 3, 2011, pp.701–705.
- [55] 20 M. Abbas, S.R. Torati, C. Kim, Nanoscale, 7, 2015, pp. 12192.
- [56] D. Kim, N. Lee, M. Park, B.H. Kim, K. An, T. Hyeon, Journal of American Chemical Society, 126, 2004, pp. 273-279.
- [57] O. Celik , M.M. Can, T. Firat, Journal of nanoparticle research, 2014, 16, pp. 2321.
- [58] Y. K. Sun, M. Ma, Y. Zhang and N. Gu, Colloids Surf A, 2004, 245, pp.15–19.
- [59] R.M. Cornell, U. Schwertmann, Wiley-VCH, Weinheim, 2003.
- [60] A.G. Roca, D. Niznansky, V.J. Poltierova, B. Bittova, G.M.A. Fernández, C.J. Serna, M.P. Morale, Journal of Applied Physics, 105, 2009, 1–7.
- [61] M. Abbas, B.P. Rao, S.M. Naga, M. Takahashi, C. Kim, Ceramics International 39 ,2013, pp. 7605–7611.
- [62] R.M. Cullity, “Introduction to Magnetic Materials”, second ed., Addison-Wesley Publishing, 1993.
- [63] G.C. Hadjipanayis, R.W. Siegel, Kluwer Academic Publishers, Dordrecht ,1994.
- [64] S. Chikazumi, “Physics of Magnetism”, John Wiley, New York, 1959.
- [65] C. Balasubramanian, Y.B. Khollam, I. Banerjee, P.P. Bakare, S.K. Date, A.K. Das, S.V. Bhoraskar, Mater. Lett. 58, 2004, pp. 3958-3962.
- [66] M. Abbas, B. P. Rao, S. M. Naga, M. Takahashi and C. Kim, Ceram. Int., 2013, 39, pp. 7605–7611.
- [67] R. M. Cullity, “Introduction to Magnetic Materials”, Addison-Wesley Publishing, 2nd edn, 1993.
- [68] G. C. Hadjipanayis and R. W. Siegel, “Nanophase Materials Synthesis - Properties – Applications”, Kluwer Academic Publishers, Dordrecht, 1994.
- [69] S. Chikazumi, “Physics of Magnetism”, John Wiley, New York, 1959.
- [70] C. Balasubramanian, Y. B. Khollam, I. Banerjee, P. P. Bakare,S. K. Date, A. K. Das and S. V. Bhoraskar, Mater. Lett. 58, 2004, pp. 3958–3962.
- [71] Y. Lv, Y. Yang, J. Fang, H. Zhang, E. Peng, X. Liu, W. Xiao and J. Ding, RSC Adv., 2015, 5, pp. 76764.
- [72] M. P. Morales, S. Veintemillas-Verdaguer, M. I. Montero,C. J. Serna, A. Roig, L. Casas, B. Martínez and F. Sandiumenge, Chem. Mater. 11, 1999, pp. 3058–3064.
- [73] Shaojun Guo and Shouheng Sun, “FePt Nanoparticles Assembled on Graphene as Enhanced Catalyst for Oxygen Reduction Reaction, JACS, 134, 2012, pp.2492-2495

- [74] Mykhaylyk O, Cherchenko A, Ilkin A, Dudchenko N, Ruditsa V, Novoseletz M and Zozulya Y Glial, “Brain tumor targeting of magnetite nanoparticles in rats” J. Magn.Magn. Mater. 225, 2001, pp. 241–247
- [75] H. Loc Nguyen, Luciano E. M. Howard, Graham W. Stinton, Sean R. Giblin, Brian K. Tanner, Ian Terry, Andrew K. Hughes, Ian M. Ross, Arnaud Serres, and John S. O. Evans, “Synthesis of Size-Controlled fcc and fct FePt Nanoparticles”, Chem.Mater. 18, 2006, pp. 6414-6424
- [76] Min Chen, Jaemin Kim, J. P. Liu, Hongyou Fan and Shouheng Sun, “synthesis of FePt nanocubes and their oriented self-assembly”, J.AM.CHEM.SOC. 128, 2006, pp.7132-7133.
- [77] H. B. Wang, H. Wang, J. Zhang, F. J. Yang, Y. M. Xu, Q. Li, “Study on Composition Distribution and Ferromagnetism of Monodisperse FePt Nanoparticles”, Nanoscale Res Lett. 5, 2010, pp. 489–493.
- [78] Thuy T. Trinh,a Derrick Mott,a Nguyen T. K. Thanhbc and Shinya Maenosono, “One-Pot Synthesis and Characterization of Well-Defined Core-Shell Structure of FePt@CdSe Nanoparticles”, RSC Advances. 1, 2011, pp. 100–108.
- [79] Shang-Wei Chou, Yu-Hong Shau, Ping-Ching Wu, Yu-Sang Yang, Dar-Bin Shieh, and Chia-Chun Chen, “In vitro and in vivo studies of FePt nanoparticles for dual modal CT,MRI molecular imaging”, J.AM.CHEM.SOC. 132, 2010, pp. 13270-13278.
- [80] Rui Hong, Nicholas O. Fischer, Todd Emrick, and Vincent M. Rotello, “Surface PEGylation and ligand exchange chemistry of FePt nanoparticles for biological applications”, Chem. Mater. 17, 2005, pp. 4617-4621.
- [81] M.Aslam, L. Fu, S. Li, Vinayak P. Dravid.”Silica encapsulation and magnetic properties of FePt nanoparticles, J. colloid and interface science, 2005, 290, pp. 444-449.
- [82] Bart-Jan Kroesen, G. Mesander, J.G. ter Haar, T.H. The and L. de Leij, Direct visualisation and quantification of cellular cytotoxicity using two colour fluorescence, J. Immunological Method, 1992, pp.156, 47-54.

## 요약문

### 바이오 응용을 위한 크기, 형태 제어가 가능한 FePt와 Ferrite 나노 입자 합성

최근 10년간 자성 나노 입자에 대한 연구가 활발하게 진행되어 왔고, 특히 바이오-메디컬 분야(자기공명영상 조영제, 발열치료, 약물전달 등)에서의 새로운 접근이 가능해지면서 많은 주목을 받고 있다. 바이오-메디컬 응용에 적합한 소재 개발이 중요한 부분으로 자리매김 하고 있고, 이에 발맞춰 다양한 자성 나노 입자의 합성은 매우 중요한 요소이며, 자성 나노 입자의 특성을 결정짓는 요소인 사이즈, 형태 등을 제어하는 기술이 핵심 연구 주제로 대두되고 있다. 본 논문에서는 바이오-메디컬 분야에서 많이 사용되고 있는 자성 나노 입자인 Ferrite( $\text{Fe}_3\text{O}_4$  and  $\text{CoFe}_2\text{O}_4$ )와 alloy 입자 (FePt, FePt/ $\text{Fe}_3\text{O}_4$ ) 합성에 대한 연구를 진행하였다. 이번 실험에서 사용되었던 열분해와 환원 반응을 통한 자성 나노 입자 합성 방법은 온도, 시간, 용매, 계면활성제, 전구체의 양 조절 등의 다양한 실험 조건으로 수-수십 나노 사이즈, 나노 입자의 형태가 미세하게 제어가 가능한 방법으로 알려져 있다. 이 방법을 통해 50 ~ 100 nm 크기의 구형, 큐브형, 육각형의 형태를 가지며 80 emu/g의 포화 자화 값을 갖는 Ferrite( $\text{Fe}_3\text{O}_4$ ,  $\text{CoFe}_2\text{O}_4$ ) 나노 입자와 5 ~ 10 nm 크기의 큐브 형태의 초상자성 alloy(FePt, FePt/ $\text{Fe}_3\text{O}_4$ ) 나노 입자를 합성하였다. 이를 X-ray diffraction (XRD), transmission electron microscopy (TEM), energy dispersive spectrometer (EDS), and Vibrating Sample Magnetometer (VSM)으로 자성 나노 입자의 형태, 특성 등을 확인하였고 THP-1 세포 생존율 테스트를 통해 농도에 따른 자성 나노 입자의 생체적합성을 확인하였다.

#### 핵심어

자성 나노 입자 합성,  $\text{Fe}_3\text{O}_4$ ,  $\text{CoFe}_2\text{O}_4$ , FePt, FePt/ $\text{Fe}_3\text{O}_4$ , 바이오 어플리케이션